Structural vulnerability of power transmission line supports: development of fragility curves for snow avalanche loads

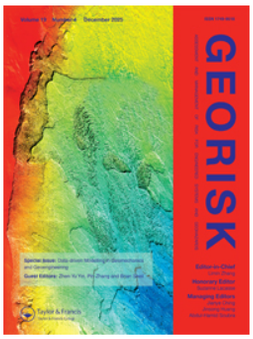

Georisk: Assessment and Management of Risk for Engineered Systems and Geohazards

ISSN: 1749-9518 (Print) 1749-9526 (Online) Journal homepage: www.tandfonline.com/journals/ngrk20

Structural vulnerability of power transmission line supports: development of fragility curves for snow avalanche loads

G. Vallero, M. Marchelli & V. De Biagi

To cite this article: G. Vallero, M. Marchelli & V. De Biagi (22 Jan 2026): Structural vulnerability of power transmission line supports: development of fragility curves for snow avalanche loads, Georisk: Assessment and Management of Risk for Engineered Systems and Geohazards, DOI: 10.1080/17499518.2026.2616777

To link to this article: https://doi.org/10.1080/17499518.2026.2616777

GEORISK
https://doi.org/10.1080/17499518.2026.2616777

Taylor & Francis
Taylor & Francis Group

Structural vulnerability of power transmission line supports: development of fragility curves for snow avalanche loads

G. Vallero [a], M. Marchelli [b] and V. De Biagi [a]

[a]Department of Structural, Building and Geotechnical Engineering, Politecnico di Torino, Torino, Italy; [b]Department of Environment, Land and Infrastructure Engineering, Politecnico di Torino, Torino, Italy

ABSTRACT

Snow avalanches pose a significant threat to power transmission lines in mountainous regions, where support structures are exposed to extreme dynamic forces. This study investigates the structural vulnerability of transmission line supports subjected to avalanche impacts, focussing on the development of fragility curves for wooden and steel poles as well as transmission towers. The analysis specifically considers both the dense snow avalanches and saltation and powder components as hazards, which exerts substantial dynamic loads on these structures. A simplified analytical approach is used for poles, while pushover FEM simulations assess the performance of transmission towers. The study evaluates the probability of failure under different avalanche flow conditions, considering a range of structural configurations with varying geometries and element sizes. The findings provide quantitative insights into the vulnerability of transmission line supports, offering a valuable tool for risk assessment, structural design, and land-use planning in avalanche-prone areas. The results emphasise the importance of incorporating avalanche-induced loads into the design of this type of infrastructure.

ARTICLE HISTORY
Received 24 April 2025
Accepted 11 January 2026

KEYWORDS
Snow avalanche hazard; failure probability; fragility curves

1. Introduction

Snow avalanches are among the most common natural hazards in mountainous regions (D. McClung and Schaerer 2006). Defined as the movement of a large mass of snow, they pose significant threats to human life, settlements, economic and tourist activities, roads, railways, structures and infrastructure in general (De Biagi, Chiaia, and Frigo 2015; Eckert et al. 2012; Mayer et al. 2008; Statham et al. 2018). In regions prone to avalanches, hazard intensity and frequency should thus be assessed by analyzing various scenarios. These scenarios serve as indicators for risk. In the field of natural hazards, and thus avalanches, risk for fixed elements is typically defined as the product of hazard and vulnerability, meaning it is a combination of the damaging event and its potential consequences (Eckert et al. 2012). The quantification of risk has several limitations and challenges, such as the selection of a frequency-magnitude relationship for events or the relationship between hazard magnitude and damage level, like a vulnerability relation (Favier et al. 2022). Addressing the physical vulnerability of a structure involves considering both the inherent properties of the exposed element and the magnitude and nature of the external forces acting upon it (Bertrand, Naaim, and Brun 2010; De Biagi, Napoli, and Barbero 2017; Glade 2003; Vallero et al. 2020).

In case of snow avalanches, the snow flow applies pressure to impacted structures, which respond based on their characteristics, geometrical configuration and material properties. Given the multi-phase nature of the phenomenon, identifying the forces acting on an affected structure is a critical task (Eckert, Naaim, and Parent 2010). The pressures exerted on obstacles can range from harmless impacts by low-intensity powder clouds to catastrophic damage from large-scale dry mixed avalanches, even leading to the collapse of reinforced concrete structures (D. McClung and Schaerer 2006). In recent decades, a wide range of numerical models have been developed to simulate avalanche dynamics, accounting for the various flow regimes that characterise these complex phenomena (Christen, Kowalski, and Bartelt 2010; Gaume et al. 2019; Li et al. 2021; Naaim, Faug, and Naaim-Bouvet 2003; Naaim et al. 2004; Sampl and Granig 2009; Sampl and Zwinger 2004). These models aim to provide detailed insights into key avalanche parameters, including velocity profiles, impact pressures, and flow depths, which are critical for understanding

CONTACT V. De Biagi valerio.debiagi@polito.it Department of Structural, Building and Geotechnical Engineering, Politecnico di Torino, Corso Duca degli Abruzzi 24, Torino 10129, Italy

avalanche behaviour and interactions with the surrounding environment. Furthermore, they serve as essential tools for hazard assessment and risk mapping in avalanche-prone areas, enabling improved land-use planning, infrastructure protection, and mitigation strategies (Gruber and Margreth 2001). As modelling techniques continue to advance, incorporating high-resolution topographical data, complex snow rheologies, and real-time weather conditions, they offer increasingly accurate predictions, supporting both engineering design and emergency response planning in regions susceptible to avalanches.

Among the infrastructures encountered by the avalanche during its propagation, power transmission lines represent ones of the most common. As infrastructures belonging to a network, these structures play a crucial role in ensuring a reliable electricity supply to remote communities, directly contributing to the safety and well-being of populations in avalanche-prone areas. Given their importance, during the design phase, structural engineers are often asked to assess the vulnerability of structures against snow avalanches and to define appropriate load profiles for snow impacts (De Biagi, Chiaia, and Frigo 2015; Hofer, Schroll, and Illmer 2019; McClung and Schaerer 1985; Thibert et al. 2008), and analyzing the behaviour of poles and towers under these extreme natural actions (Caviezel et al. 2021). Despite their potential to cause severe structural damage, current design standards rarely account for extreme dynamic actions of such type. The technical guidelines on the management and mitigation of avalanche risk (Campbell et al. 2016; Margreth 2007) report the principles and suggest formulae, but they are not specific for such structural systems. Based on the multitude of incidents occurred in the Rockies since the Sixties, British Columbia Power Authority has conceived and implemented some design principles to mitigate the interaction between the natural phenomenon and the power transmission lines, providing robustness to the system (Lu and Chakrabarti 2022).

The typical damages observed on power transmission poles/towers impacted by snow avalanche range from the local conductor release, to the failure of the structure. Figure 1 shows two power transmission structures damaged by avalanches. The failure modes consist in the formation of a plastic hinge for steel poles, bending/shear failure for timber (wooden) poles, or the collapse of the taller lattice towers due to the propagation of a local damage (buckling or failure in bending).

Avalanche-induced loads can affect different parts of the support structures, depending on the flow regime (Barbero et al. 2013; Maggioni et al. 2019). The dense core primarily impacts the lower sections of poles and towers, while the powder cloud component can reach the medium-upper parts of the structures (Bartelt et al. 2020; Caviezel et al. 2021). Such structures exhibit uneven mass distribution, with a significant portion of the supported load concentrated near the top, making them particularly susceptible to dynamic loads and instability. Beyond direct structural impact, powder avalanches can also exert high instantaneous pressures on the conductors suspended between towers, further increasing the probability of failure (Gorynina and Bartelt 2023; Jones et al. 2003). As a result, tall poles and lattice towers are subjected to both direct impact and indirect effects, making them particularly vulnerable to avalanche-induced damage. Understanding their mechanical response to avalanche forces is essential for risk assessment and land management purposes. Assessing structural vulnerability to natural hazards is thus a crucial issue that must be addressed during the design phase for new installations or checked for existing power lines (Jakob, Stein, and Ulmi 2012; Van Westen, Castellanos, and Kuriakose 2008; Zhang, Xu, and Wang 2024). In assessing the failure, the uncertainties associated to the phenomenon, to the material properties, or to the geometry must be included in the analysis. For this purpose, fragility curves are usually developed. Although largely adopted in the seismic engineering (Rajkumari, Thakkar, and Goyal 2022), their formulation can be easily adopted for other natural hazards (Anisha et al. 2022; Wojciechowska et al. 2015). Given a specific level of damage, say the collapse, the curves describe the conditional probability to manifest this damage given a hazard of a certain magnitude, here the snow avalanche pressure (Ousset et al. 2015). The fragility curves represent an easy and comprehensive tool to develop damage scenarios on complex systems, such as power networks (Dunn et al. 2018), in particular when the redundancy is low.

The fragility curves can be obtained from the back-analysis of existing faults, or from modelling and direct calculations. Due to the limited number of well-documented events of impacted power transmission structures, the latter option is here selected. Focussing on the effects of dense-core avalanches impacting the support structures, firstly, this study aims at investigating the structural vulnerability of power transmission structures. This serves to determine the fragility curves associated to the failure of wooden and steel poles, and power transmission towers. The poles were considered to be made from two distinct materials: steel, representing modern Italian infrastructure, and wood, reflecting older, traditional support systems, still in use. For the transmission towers, typical support structures are considered.

Figure 1. In (a), collapse of a steel pole due to the impact of a snow avalanche in Cogne, Aosta Valley, Italy, ref. snow avalanche no. V-12-121 on Dec 15, 2008. In (b), collapse of a power transmission tower due to the impact of a snow avalanche in Valsavarenche, Aosta Valley, Italy, ref. snow avalanche no. V-13-88 on Dec 8, 2018. The photos are publicly accessible at (RAVA, Ufficio Neve e Valanghe 2025).

The paper is structured as follows. Section 2 provides an overview of snow avalanches, with a focus on their flow regimes and impact mechanisms, fundamental to understand the complexity of the phenomenon and the consequent assumptions behind the pressure calculations. It details, the distinction between dense-core, powder-cloud, and mixed avalanches is provided, analyzing their effects on structures. In Section 3, the methodology adopted in this study is presented, outlining the key assumptions and simplifications, as well as the different analytical and numerical approaches used to evaluate the structural capacity of poles and transmission towers. Section 4 discusses the results of the analyses, including the development of fragility curves to quantify the probability of failure under varying avalanche conditions. Finally, Section 5 summarises the main findings, draws conclusions, and proposes potential directions for future research.

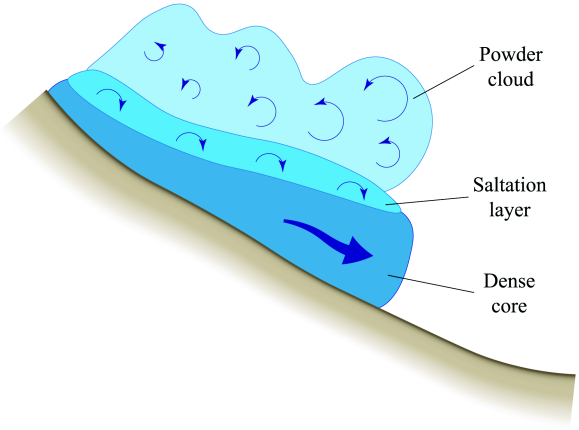

Figure 2. Scheme of the three distinct layers forming a typical mixed dry-snow avalanche.

2. Snow avalanches

2.1. Avalanche flow regimes

The downhill dry-snow avalanche flow is a complex phenomenon, significantly influenced by the topographical features and surface characteristics of the terrain, as well as by any obstacles encountered along the descent (Ancey 2016; Pudasaini and Hutter 2007). Avalanches typically affect snow-covered slopes, where the erosive action of the flow accumulates additional mass as it progresses, thereby increasing both the volume and intensity of the avalanche (Hopfinger 1983). Dry-snow avalanches are typically classified into three regimes: dense-core flow, powder cloud, and mixed avalanches (Caviezel et al. 2021; Gauer et al. 2008). The dense-core flow consists of a compact mass of snow moving along the slope, while the powder cloud is a low-density mixture of ice crystals and air. The mixed avalanche, the most common type, combines characteristics of both the dense core and the powder cloud (Mellor 1978), as shown in Figure 2. the dense avalanche core and the powder cloud . It consists of clumps and blocks of snow with medium density (200 kg m^{-3}), often reaching increasing up to 500 kg m^{-3} if other materials, such as wooden debris, rocks or ice are entrained (Caviezel et al. 2021; McClung and Schaerer 2006). The core is responsible for the majority of the avalanche's destructive power due to its mass and the high pressure it exerts on the obstacles. As a surface flow, the dense core is strongly influenced by the terrain it moves over and its characteristics, such as steepness, surface roughness, vegetation, channels, etc. The interaction of the flow with the ground results in additional snow accumulation, further increasing mass and momentum.

The powder cloud is the external part of the avalanche flow and consists of fine ice particles and dust, generated when dense snow and ice fragments are ejected from the avalanche core into the air (Schweizer, Bartelt, and van Herwijnen 2021). Larger particles eventually return to the core, while the smaller ones remains airborne, creating a natural separation between the core and cloud. As the cloud forms, it is continuously supplied from the core and can reach high speeds. Unlike the core, which follows the terrain, the airborne cloud moves independently of the surface, travelling initially in the direction provided by the initial momentum. The cloud can detach from the dense core, extending its trajectory into more distant areas, making its dynamics difficult to predict and its evolution extremely hazardous. It can reach depths of tens of meters and contains a significant volume of air, often exceeding 90%, with an exceptionally low density of less than 10 kg m^{-3} (McClung and Schaerer 2006).

In mixed dry-snow avalanches, which feature both a dense core and a powder cloud without a clear dominance of either, there exists an intermediate-density layer, known as the saltation layer. This layer, with a density ranging from 30 kg m^{-3} to 100 kg m^{-3}, forms between the dense core and the powder cloud. Here, snow particles are briefly lifted from the surface and then fall back, undergoing a bouncing or saltation motion similar to that observed in wind-blown sand transport (Nishimura et al. 1989). In the saltation layer, snow and ice particles move at high velocities, and their continuous interaction with the terrain can contribute to snow erosion and the transport of additional material within the avalanche flow, thereby increasing its mass and energy (Gauer et al. 2008).

Wet-snow avalanches are instead characterised by a dense core, only, reaching densities up to 500 kg m^{-3} and slower velocities in the range of 20m s^{-1} to 100m s^{-1} (McClung and Schaerer 2006).

2.2. Avalanche-obstacle interaction forces

2.2.1. Dense-core avalanches

In case of a dense-core avalanche impacting a large obstacle, the majority of the flow will be obstructed by the structure, exerting dynamic pressure on the exposed surface, with only a small portion of the flow diverting around it. The pressure can be analytically computed according to the following simple relationship (Hopfinger 1983; Jóhannesson et al. 2009; Mellor 1978):

$$p_f = \kappa_{dyn}\, \rho_f\, v_f^2, \tag{1}$$

where ρ_f represents the flow density, v_f is the flow velocity, and κ_{dyn} is a dimensionless dynamic coefficient. In the case of static equivalent pressure, $\kappa_{dyn} = 1$, whereas for peak dynamic pressure estimation, κ_{dyn} takes values greater than 1 to account for dynamic amplification effects.

For dense-core avalanches that impact small (tight) obstacles, the formulation of the pressure is quite similar to the previous one (Kyburz 2021; Rudolf-Miklau, Sauermoser, and Mears 2014):

$$p_f = \frac{1}{2}\, \kappa_{dyn}\, c\, \rho_f\, v_f^2, \tag{2}$$

where c is a dimensionless shape coefficient that takes into account the form of the impacted element. In Table 1, some values of c are reported with reference to some typical obstacle shapes and types of avalanche.

When a dense-core avalanche impacts an obstacle, the dynamic force of the collision causes part of the flow to ascend along the exposed surface of the obstacle, reaching a height beyond the original avalanche flow depth, known as climbing (or stagnation) height (h_{dyn}), which is given by the following relationship (Rudolf-Miklau, Sauermoser, and Mears 2014):

$$h_{dyn} = \frac{v_f^2}{2\, g\, \lambda}\, f_r, \tag{3}$$

where g is the gravitational acceleration, λ is a dimensionless coefficient that accounts for the loss of momentum during the impact, and f_r is a dimensionless correcting factor accounting for the shape of the impacted element. For dry-snow avalanches, $\lambda = 1.5$, while for wet-snow avalanches, λ typically ranges from 2 to 3. The coefficient f_r is related to the ratio between the width of the obstacle (b), measured in the direction normal to the flow trajectory, and the height of the avalanche flow (h_f). In Table 2, representative values of f_r are provided.

Table 1. Values of the shape coefficient c for dense-core snow avalanche with reference to some typical shapes of the obstacle.

Shape of the obstacle	Dry-snow avalanche	Wet-snow avalanche
Circular cylinder	1.5	3 to 5
Rectangle	2	4 to 6
Triangular wedge	1.5	3 to 6

Table 2. Values of the correcting factor f_r with reference to the ratio between the width of the obstacle (b) and the height of the avalanche flow (h_f).

$\frac{b}{h_f}$	0.1	0.5	1	2	≥ 3
f_r	0.1	0.4	0.7	0.9	1

Table 3. Values of the shape coefficient c for the powder-cloud and saltation layers with reference to some typical shapes of the obstacle.

Shape of the obstacle	Powder-cloud layer	Saltation layer
Circular cylinder	1	1
Rectangle	1.5	2
Triangular wedge	1.2	1.5

Finally, the impact force, Q, can be assessed by integrating the pressure over the impacted area, Σ:

$$Q = \int_{\Sigma} p_f \, d\Sigma. \tag{4}$$

2.2.2. Powder-cloud avalanches

In assessing the pressures exerted by powder-cloud avalanches, it is essential to account for the fact that the saltation and suspension layers exhibit significantly lower densities compared to dense-core avalanches. However, their substantially higher velocities compensate for this reduced density, contributing to considerable impact forces. Also for powder-cloud avalanches, the pressure of the flow can be estimated by means of Equations (1) and (2), depending on the width of the impacted element. In Table 3, the values of c for powder-cloud avalanches are reported.

2.2.3. Mixed avalanches

To estimate the forces exerted by each layer, it is often assumed that the layers are distinctly separated, enabling independent evaluation of the impact actions (Kyburz 2021; D. McClung and Schaerer 2006; Sovilla, Schaer, and Rammer 2008). This simplifies the complex dynamics by isolating the contributions of each component. The forces for each layer are calculated using the same principles applied to dense-core and powder-cloud avalanches, ensuring that the unique characteristics of each are properly considered in the assessment of impact pressures. In addition to the contributions from the three avalanche layers, the load from the pre-existing snow-cover on the slope can also be transferred to the impacted structure. A sketch illustrating the forces exerted by a mixed avalanche is shown in Figure 3.

3. Methodology

3.1. Assumptions and simplifications

To assess the mechanical behaviour of these structures, different approaches and assumptions were applied based on the specific characteristics of each structure. For poles, a simplified analytical method was employed, while towers were analysed using a FEM approach.

Snow avalanches are inherently variable phenomena. Multiple events may occur along the same path within a single season, each characterised by distinct

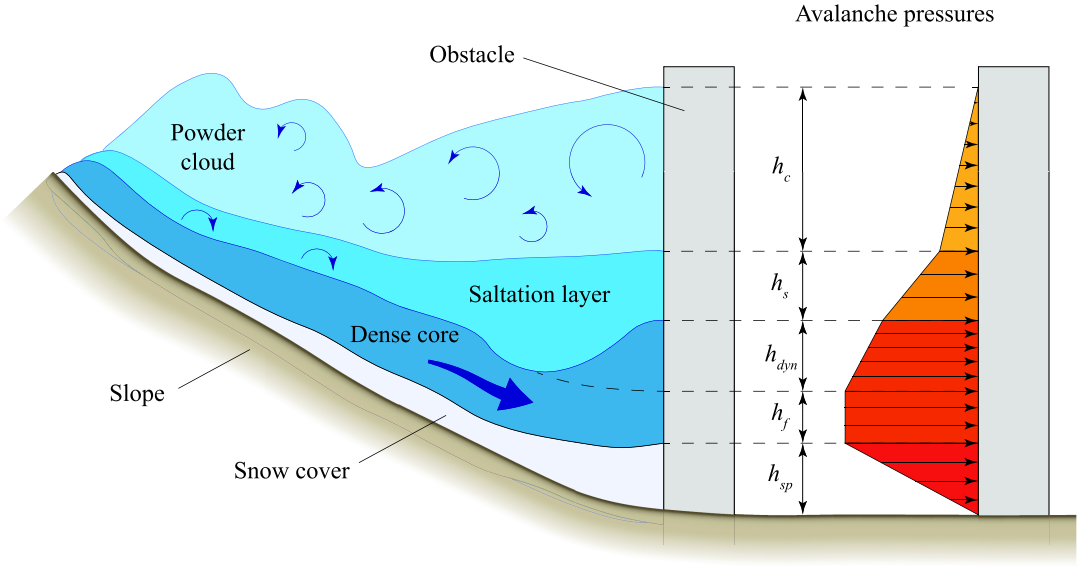

Figure 3. Representation of the actions exerted by a mixed avalanche on an obstacle. On the left, a scheme of the three different layers composing the avalanche flow is reported. Note the climbing height (h_{dyn}) induced by the dynamic impact of the dense core on the obstacle. On the right, the shape of the pressures exerted by the avalanche is reported with reference to the same obstacle.

release volumes, snow types (e.g. dry or wet), and flow regimes. These initial conditions, combined with the spatial variability of snow cover along the track, lead to a wide range of flow velocities and bulk densities at the point of impact with the obstacle. Given this variability, flow velocity alone does not provide a sufficiently robust metric for characterising avalanche loading. In contrast, impact pressure, defined as a function of both velocity and density, offers a more comprehensive representation of the dynamic load exerted by the avalanche and constitutes the most physically robust descriptor of the dynamic load imposed by avalanches.

In both cases, avalanche intensity is assumed to depend on three key variables: dense-flow pressure (p_f), flow depth (h_f), and powder/saltation pressure (p_s). Specifically, our analyses on poles focus on a dense-core avalanche moving along the slope. Different snow conditions are considered, including dry- and wet-snow avalanches. The former may be accompanied by a saltation layer, which increases interaction with electrical structures and cables. Analyses on towers address both dense-core avalanches and powder-snow avalanches.

The following study is based on static loading assumptions. However, due to the transient nature of avalanche-obstacle interactions, the forces acting on structures can be significantly larger. This increase is accounted for by the term κ_{dyn} in Equations (1) and (2), which serves as a dynamic amplification factor. Consequently, the pressure values obtained in the static analysis can be adapted to a transient scenario by dividing them by κ_{dyn}.

3.2. Poles

3.2.1. Dense-core avalanches

Figure 4 summarises the geometry of the problem. The impact force is calculated for the flow depth (h_f) assuming a rectangular distribution of pressure, while a triangular distribution is applied for the climbing height (h_{dyn}). The two forces (Q^a for the flow depth and Q^b for the climbing height) can be determined using Equation (4), where the area of the impacted surface (Σ) is dependent on the shape of the pole. Therefore, assuming the pole as a vertical cantilever fixed at the ground level, the design values for the maximum bending moment and shear force are given by the following relationships:

$$M_{Ed} = M_{\max} = Q^a \left(h_{sp} + r_a\right) + Q^b \left(h_{sp} + r_b\right), \quad (5)$$

$$V_{Ed} = V_{\max} = Q^a + Q^b, \quad (6)$$

in which r_a and r_b are the two distances between the snow cover surface and the application point of the impact forces Q^a and Q^b, while h_{sp} is the thickness of the snow cover.

In the analysis, the avalanche flow is characterised by depths ranging from 0.5 to 5 m and densities (ρ_f) between 200 kg m^{-3} to 500 kg m^{-3} (McClung and Schaerer 1985; McClung and Schaerer 2006). These values were selected as representative of the possible range encountered in the Alpine region. In addition, the presence of *in-situ* snow layer of thickness ranging from 0 to 1 m was considered. Specifically, ten values of flow depth were considered in the range with 0.5 m step. Ten different density values equally spaced in the considered range and ten different *in-situ* snow layer

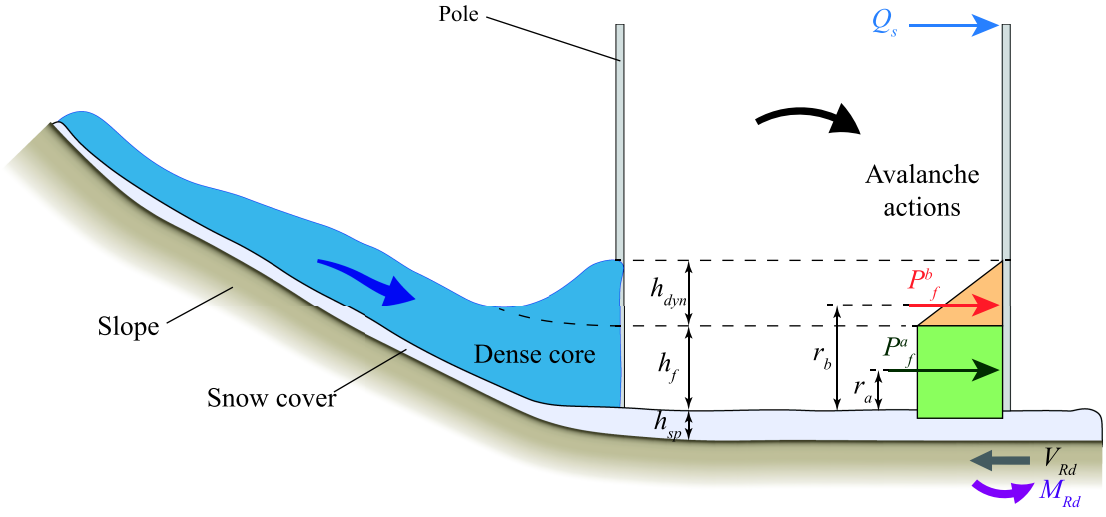

Figure 4. Representation of the analytical model used to represent the flow action on wooden and/or steel poles. The snow present in the rear of the pole is not reported in the rear of the pole for sake of clarity.

Table 4. Values of D and t for the analysed poles.

Type of support	Quantity	Value
Steel poles	Diameter, D (mm)	from 150 to 350 at 20 mm increments
	Thickness, t (mm)	from 5 to 15 at 2 mm increments
Wooden poles	Diameter, D (mm)	from 150 to 300 at 10 mm increments

of thicknesses in the above mentioned range were included in the simulations. The snow avalanche pressure ranged from 0.5 to 250kPa with 300 logarithmically spaced intervals.

A tubular cross section was considered for the steel poles with external diameter D and thickness t. For wooden poles, a circular cross section was adopted with diameter D. To explore the effects of varying geometries, multiple values for D and t were tested, as summarised in Table 4.

For each pressure level, the total number of combination of the input parameters, i.e. flow densities, *in-situ* snow depth, and pole diameter was 1100 and 1600, for steel and wooden poles, respectively.

For each case, the value of the flow velocity v_f was calculated with Equation (1), together with the climbing height h_{dyn}, from Equation (3). The adopted value of λ ranged between 1.5 and 3.0, to consider the type of expected flow (dry or wet). The two forces Q^a and Q^b were defined together with the maximum moment (M_{Ed}) and shear (V_{Ed}) by means of Equations (5) and (6). These represent the impacting actions.

The resisting bending moment and shear of the poles were calculated following the European guidelines (Steer 2001) and the Italian construction standards (Gazzetta Ufficiale della Repubblica Italiana 2018). In the analysis of the steel pole, only the S235 steel class ($f_{yk} = 235$ MPa for a thicknesses smaller than 40 mm) was considered. Five different strength classes were considered for the wooden poles, representative of the timbers that can be found in the Alpine area. The flexural and shear characteristics strengths are reported in Table 5.

The strength design values were obtained by dividing the characteristic value by material's partial safety factors, equal to 1.05 for steel and 1.50 for timber. The timber strength was multiplied by 1.1 to account for the duration of the load (instantaneous).

Table 5. Timber classes adopted in the study.

EN 338 class (CEN 2016)	Fir C18	Fir C24	Pine C15	Pine C22	Chestnut
Flexural strength, $f_{m,k}$ (MPa)	18	25	15	22	28
Shear strength, $f_{v,k}$ (MPa)	3.4	4.0	3.0	3.8	4.0

The bending capacity was computed with the classical Navier formula, while for the shear capacity the equivalent shear area approach was adopted (Gazzetta Ufficiale della Repubblica Italiana 2018).

Given a value of pressure and height, the capability of the pole to withstand each value of action was assessed for all the different geometrical configurations. The pole is deemed capable of resisting the avalanche forces if both of the following inequalities are satisfied:

$$M_{Rd} > M_{Ed}, \tag{7}$$

$$V_{Rd} > V_{Ed}. \tag{8}$$

Considering the different thicknesses of the tubular steel pole, the total number of combinations related to the steel poles increases to $n_{tot} = 5500$, accounting for the different flow densities and *in-situ* snow depth. On the contrary, considering the 5 different strength classes of timber, the total number of combinations related to the timber poles is $n_{tot} = 8000$.

For each pressure and height value, the probability of failure (P_f) is defined as the ratio of the number of cases where at least one of the two previous inequalities is not satisfied (n_f) to the total number of investigated cases (n_{tot}), i.e. the number of different geometrical configurations:

$$P_f(p_f, h_f) = \frac{n_f}{n_{tot}}. \tag{9}$$

3.2.2. Saltation layer in dry-snow avalanches

Power lines with poles can be subjected to the force caused by the saltation layer in dry-snow avalanches. Such layer interacts not only with the pole, but also with the cable, causing extra horizontal forces on the supporting system. This latter interaction has the strongest influence as the span of the cable, i.e. the distance between subsequent poles, can be large. To account for such actions, an additional force Q_s is applied on the top of the pole, which height is deterministically set at 10 m as reported by many producers. The force is the product of the pressure exerted by the saltation layer p_s, the diameter and the width of the saltation layer, presupposing that the layer not necessarily interacts with the whole span between two cables. Different scenarios are considered: (i) the absence of the dense component on the presence of the saltation layer, only, (ii) the simultaneous presence of dense and saltation components, the former with different flow depths.

The force Q_s increments the acting bending moment M_{Ed} and the shear V_{Ed}, as an additional term in Equations (5) and (6), making the system more prone to failure. In the analysis, the pressure induced by the saltation layer ranges between 0 to 15kPa in 20 steps of

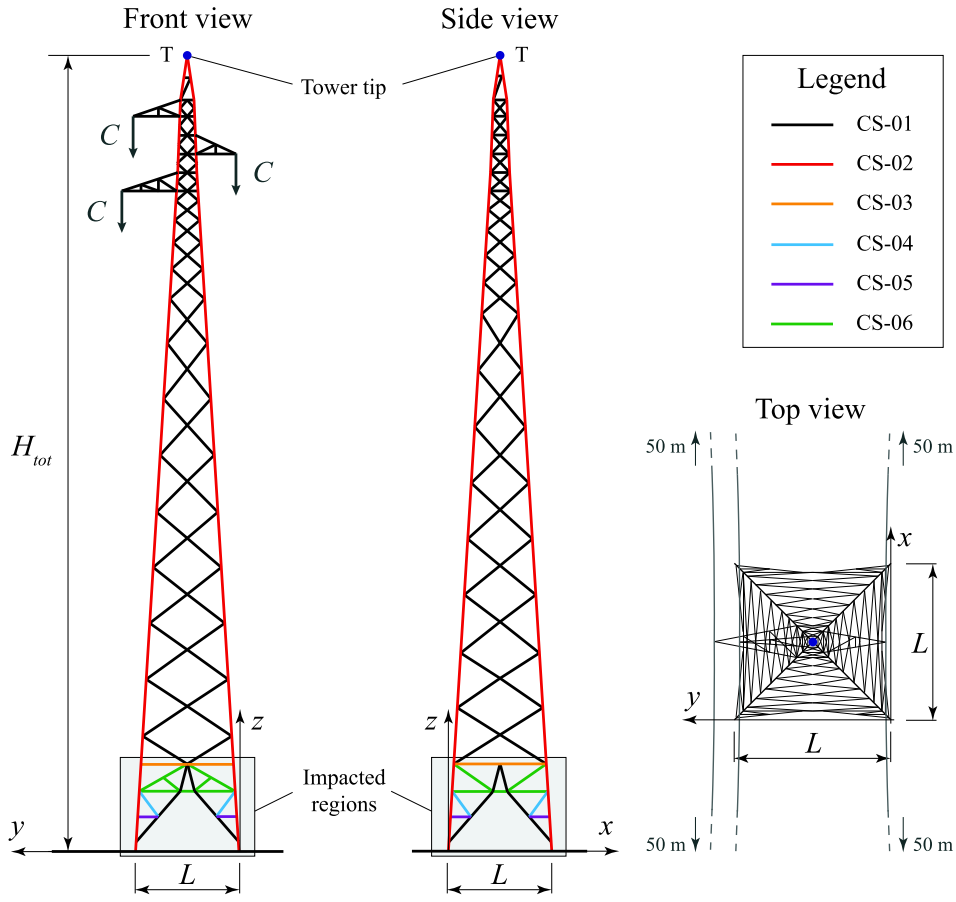

Figure 5. Scheme of the analysed tower. The front and side views illustrate the different steel beams used in various parts of the structure. The gray rectangles highlight the regions impacted by avalanches.

0.75kPa. The diameter of the cable is set equal to 30 mm, to account for multipole braided cables, and the interaction width ranges between 5 to 40 m, with steps of 1.75 m. Four dense component flow depths are analysed: 0.5 m, 1.5 m, 2.5 m and 3.5 m, plus the case of absence of the dense component. Recalling that the saltation layer mainly forms in dry-snow avalanches, the climbing height was computed considering λ equal to 1.5.

3.3. Power transmission towers

For high- or medium-voltage power transmission lines, lattice towers are typically used. The geometry of support towers commonly employed by Italian electricity companies was adopted as representative. A tower with a total height of $H_{tot} = 42.5$ m and a square base with side length $L = 5.5$ m was firstly analysed. The types of the adopted steel profiles are shown in Figure 5 and Table 6, where the L-shaped profiles are names as 'L', followed by the cross-section external dimensions and thickness (in mm). The tower consists of structural steel belonging to two different grades, i.e. S235 and S335. The mechanical properties of both the steels are summarised in Table 7.

To account for potential variations in the dimensions of power transmission towers, we analysed both smaller

Table 6. Beams adopted for the transmission tower and their cross-section and material specifications. All profiles are L-shaped and the dimensions of the L is reported in mm in the names.

ID	Profile	Type of steel
CS-01	L70×70×6	S235
CS-02	L130×130×11	S355
CS-03	L100×100×6	S235
CS-04	L40×40×4	S235
CS-05	L45×45×4	S235
CS-06	L90×90×6	S235

Table 7. Mechanical properties of the materials considered in this work.

Property	Type of steel	
	S235	S355
Young modulus (E)	210*GPa*	210 GPa
Density (ρ)	7850 kg m^{-3}	7850 kg m^{-3}
Poisson's ratio (ν)	0.3	0.3
Characteristic yield stress (σ_{yk})	235 MPa	355 MPa
Characteristic ultimate stress (σ_{uk})	360 MPa	510 MPa
Yield strain (ε_{yk})	0	0
Ultimate strain (ε_{uk})	0.178	0.178

Table 8. Scaling factors used in this work and consequent dimensions of the scaled towers.

Tower size	Scaling factor (SF)	L (m)	H_{tot} (m)
Small (SML)	0.6	3.3	42.5
|	0.8	4.4	42.5
Medium (MED)	1.0 (original)	5.5	42.5
Large (LAR)	1.2	6.6	42.5
|	1.4	7.7	42.5

and larger towers. Specifically, we scaled the lateral dimensions of the original tower with four different scaling factors (SF), while keeping the total height (H_{tot}) constant. The considered scaling factors were SF = 0.6, 0.8, 1.2, and 1.4, in addition to the original value of SF = 1.0, which represents the baseline structure. The resulting towers were grouped in three classes based on the size: small class (SML) relates to SFs 0.6 and 0.8, medium class (MED) to SF equal to 1.0, large class (LAR) to SFs 1.2 and 1.4. The sizes of the 5 resulting towers are reported in Table 8.

All the structures (corresponding to the five values of SF) are subjected to their self-weight and to the self-weight of the cables $C = 5$ kN (spanning 50 m on each side of the tower), as shown in Figure 5.

3.3.1. Dense-core avalanches

The avalanche impact was modelled as an equivalent static force, represented by a uniformly distributed linear load applied directly to the profiles of the tower. Given the level of detail in the analysis, the applied force does not account for the profile's shape. This choice is based on the observation that moving snow tends to accumulate against flat surfaces, forming a wedge-like deposit that alters the geometry of the impacted profile. Consequently, the interaction dynamics are primarily governed by this modified shape rather than by the initial impact direction. It was assumed that only the base of the tower could be impacted by the avalanche, as highlighted in Figure 5. Three avalanche flow depths (h_f) were considered, that are: $h_{f,1} = 1.85$ m, $h_{f,2} = 3.2$ m, and $h_{f,3} = 4.7$ m, corresponding to the first three levels of the tower Figure 5.

Referring to the top view shown on the right in Figure 6, three primary avalanche flow directions (AF) were considered. According to the x–y reference system as reported in Figure 6, the first direction, AF-1, is oriented along the x-axis, the second, AF-2, is oriented along the y-axis, and the third direction, AF-3, is oriented along the bisector of the x-y quadrant. These three flow directions were combined with the three defined flow depths and the twelve impact areas shown in Figure 6, resulting in a total of 36 different load cases for each scaling factor SF, as summarised in Table 9, representing a wide variety of impacting scenarios. Considering all five SF values, a total of n_{tot} =180 load cases were analysed.

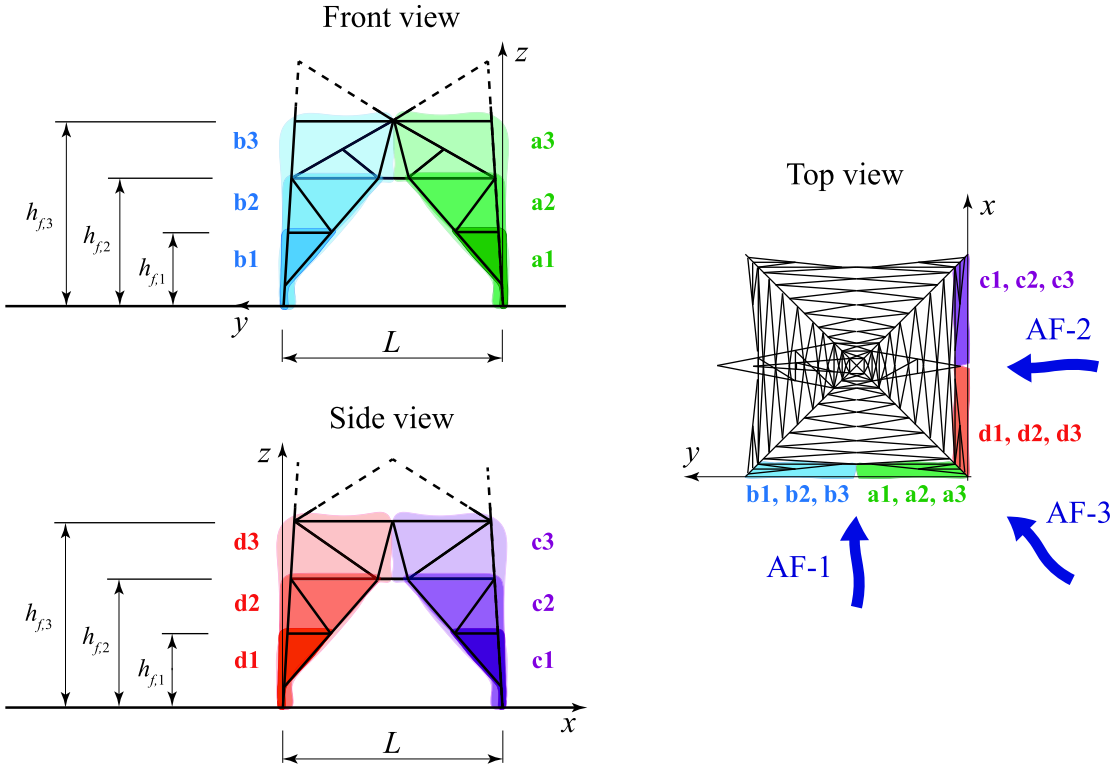

Figure 6. Representation of the loaded regions with reference to the different load cases.

The failure mechanisms of power transmission towers are complex and not always traceable to a single phenomenon (Kim et al. 2025; Tapia-Hernández, Ibarra-González, and De-León-Escobedo 2017; Yu et al. 2022). For slender lattice structures, usually, elements' buckling represents the main cause of local failure. Anyway, due to the mutual connections between the elements, redistribution mechanisms originate when an element fails, resulting that the local failure is not as critical as the complete collapse of the tower. The back-analysis of the failure of transmission towers highlighted that, despite the buckling of bracing members, the collapse suddenly occurs when the leg members undergo failure (Albermani, Kitipornchai, and Chan 2009). The structural performance of the tower was evaluated through a numerical model developed using the FEM software Abaqus/Standard (Dassault Systemes Simulia Corporation 2011). The geometry of the different scaled towers was reproduced by means of an assembly of two-node beam elements (B31 in Abaqus terminology) to which the mechanical and cross-sectional propertiens of each profile were asssigned. An equivalent dynamic implicit approach was adopted to simulate the avalanche load on the impacted regions, according to the defined load cases (Table 9).

Since an elastic analysis does not account for the redistribution of forces during progressive yielding and can fail in predicting the failure mechanisms in complex structure, a non-linear static pushover analysis was performed. Considering the inelastic behaviour of the structure, this approach can thus provide accurate predictions of the performance of the structure beyond the elastic limit. This approach is usually adopted in progressive collapse studies (Kiakojouri et al. 2020, 2023) as it enables the evaluation of overall structural behaviours together with the investigation of the sequential formation of plastic hinges within the individual structural elements that constitute the entire structure. The plot of the displacement of a control point over the load reveals a transition between linearity and non-linearity (Cai et al. 2019; Fu et al. 2019).

In the present case, the tower top is assumed as control point. Based on the analysis of previous failures (Albermani, Kitipornchai, and Chan 2009; Rao et al. 2010) and on the studies on fragility modelling on such lattice systems (Fu et al. 2019; Zhang et al. 2015), the collapse of the tower was considered to happen when one of the following conditions is satisfied:

- the horizontal displacement of tower tip exceeds a given threshold. Based on previous studies (Cai et al. 2019; Zhang et al. 2015), the threshold can be set at 1/100 of tower's height, i.e. 0.425 m;
- the force in any of leg members (profiles CS-02) exceeds the buckling force (in compression) or the capacity (in tension).

Table 9. Load cases considered for simulating the avalanche load on the analysed power transmission tower.

ID	Avalanche flow depth	Impacted regions	Avalanche flow direction (load case)
1	$h_{f,1}$	a1+b1	AF-1 (A-$h_{f,1}$)
2	$h_{f,2}$	a1+a2+b1+b2	AF-1 (A-$h_{f,2}$)
3	$h_{f,3}$	a1+a2+a3+b1+b2+b3	AF-1 (A-$h_{f,3}$)
4	$h_{f,1}$	a1	AF-1 (A1-$h_{f,1}$)
5	$h_{f,2}$	a1+a2	AF-1 (A1-$h_{f,2}$)
6	$h_{f,3}$	a1+a2 +a3	AF-1 (A1-$h_{f,3}$)
7	$h_{f,1}$	b1	AF-1 (A2-$h_{f,1}$)
8	$h_{f,2}$	b1+b2	AF-1 (A2-$h_{f,2}$)
9	$h_{f,3}$	b1+b2+b3	AF-1 (A2-$h_{f,3}$)
10	$h_{f,1}$	c1+d1	AF-2 (B-$h_{f,1}$)
11	$h_{f,2}$	c1+c2+d1+d2	AF-2 (B-$h_{f,2}$)
12	$h_{f,3}$	c1+c2+c3+d1+d2+d3	AF-2 (B-$h_{f,3}$)
13	$h_{f,1}$	c1	AF-2 (B1-$h_{f,1}$)
14	$h_{f,2}$	c1+c2	AF-2 (B1-$h_{f,2}$)
15	$h_{f,3}$	c1+c2+c3	AF-2 (B1-$h_{f,3}$)
16	$h_{f,1}$	d1	AF-2 (B2-$h_{f,1}$)
17	$h_{f,2}$	d1+d2	AF-2 (B2-$h_{f,2}$)
18	$h_{f,3}$	d1+d2+d3	AF-2 (B2-$h_{f,3}$)
19	$h_{f,1}$	a1+b1+c1+d1	AF-3 (C-$h_{f,1}$)
20	$h_{f,2}$	a1+a2+b1+b2+c1+c2+d1+d2	AF-3 (C-$h_{f,2}$)
21	$h_{f,3}$	a1+a2+a3+b1+b2+b3+c1+c2+c3+d1+d2+d3	AF-3 (C-$h_{f,3}$)
22	$h_{f,1}$	c1	AF-3 (C1-$h_{f,1}$)
23	$h_{f,2}$	c1+c2	AF-3 (C1-$h_{f,2}$)
24	$h_{f,3}$	c1+c2+c3	AF-3 (C1-$h_{f,3}$)
25	$h_{f,1}$	a1+d1	AF-3 (C2-$h_{f,1}$)
26	$h_{f,2}$	a1+a2+d1+d2	AF-3 (C2-$h_{f,2}$)
27	$h_{f,3}$	a1+a2+a3+d1+d2+d3	AF-3 (C2-$h_{f,3}$)
28	$h_{f,1}$	b1	AF-3 (C3-$h_{f,1}$)
29	$h_{f,2}$	b1+b2	AF-3 (C3-$h_{f,2}$)
30	$h_{f,3}$	b1+b2+b3	AF-3 (C3-$h_{f,3}$)
31	$h_{f,1}$	a1+c1+d1	AF-3 (C4-$h_{f,1}$)
32	$h_{f,2}$	a1+a2+c1+c2+d1+d2	AF-3 (C4-$h_{f,2}$)
33	$h_{f,3}$	a1+a2+a3+c1+c2+c3+d1+d2+d3	AF-3 (C4-$h_{f,3}$)
34	$h_{f,1}$	a1+b1+d1	AF-3 (C5-$h_{f,1}$)
35	$h_{f,2}$	a1+a2+b1+b2+d1+d2	AF-3 (C5-$h_{f,2}$)
36	$h_{f,3}$	a1+a2+a3+b1+b2+b3+d1+d2+d3	AF-3 (C5-$h_{f,3}$)

Note: All 36 load cases were applied across the five scaling factors (SF), resulting in a total of 72 cases for SML and LAR tower types and 36 cases for MED case. In the last column, the abbreviations shown in brackets will be used hereafter to refer to the corresponding load cases or groups of load cases. $h_{f,1}$, $h_{f,2}$, and $h_{f,3}$ refer to the first three levels of the tower.

The avalanche load was assumed as a time-dependent force, increasing linearly over the fictitious time at a rate of 950 kN/s, as illustrated in Figure 7. It was applied during the second time step, following an initial step in which only the gravity load (i.e. the dead load of the structure and the weight of the cables) was considered. The first time step has a fixed duration of 1 s, while the second one varies depending on when each analysis reaches the ultimate failure conditions. This approach provides a detailed time-history of the mechanical response of the entire system throughout the

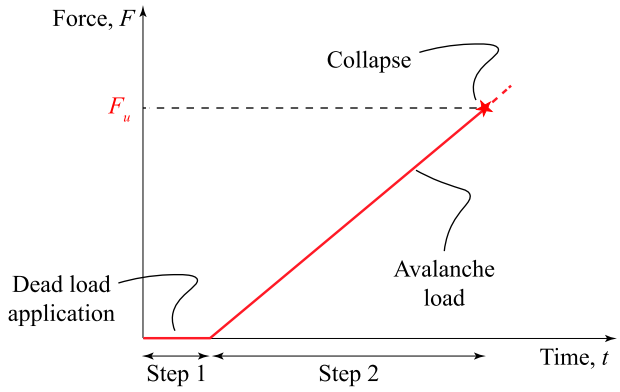

Figure 7. Application of the equivalent avalanche load to the tower model in Abaqus. The linear load applied to the beams was linearly increased during step 2 until the collapse of the tower, when the analysis was stopped.

loading process. For a given flow depth h_{f_i} ($i = 1, 2, 3$), a set of 36 or 72 values (for MED, or for SML and LAR towers, respectively) of the ultimate force that activates one of the two failure conditions was obtained. The corresponding pressure was determined as the ratio of the force over the area defined by the profile. The values were sorted from minimum to maximum and a failure probability was assigned to each on the basis of the index position j on the sorted list:

$$P_f(h_{f_i}) = \frac{j}{\max j + 1}. \tag{10}$$

3.3.2. Powder avalanches

The impact was modelled in the finite element (FEM) software as a uniform line load applied to the structural elements along one face of the tower. Three powder-flow depths were considered: one-third, two-thirds, and the full tower height (H_{tot}). The loading procedure follows the methodology previously adopted for dense-core avalanche simulations, involving a progressively increasing lateral load from zero to a nominal value: 20 kN/m for the 1/3 and 2/3 cases, and 1 kN/m for the full-height case (3/3). The collapse criteria defined for dense-core avalanches were consistently applied in these analyses. Three flow directions, AF-1, AF-2, and AF-3, were examined, as illustrated in Figure 6. For each height, the maximum pressures corresponding to the three directions were interpolated as a function of impact angle using a sine-like relationship. Similarly, pressures computed at the three flow depths (1/3, 2/3, and 3/3 of H_{tot}) were interpolated across depth using an exponential-like function. Based on the maximum pressure values, failure probability curves were derived through Monte Carlo sampling of flow depth and impact angle for the following scenarios:

- flow depth in the range $(0.45-0.55)H_{tot}$ and impact angle in the range $0°-90°$;
- flow depth in the range $(0.70-0.80)H_{tot}$ and impact angle in the range $0°-90°$;
- flow depth in the range $(0.95-1.05)H_{tot}$ and impact angle in the range $0°-90°$;
- flow depth equal to $1.5H_{tot}$ and impact angle in the range $0°-90°$, to represent flow depths larger than H_{tot}.

The analysis was limited to towers belonging to the medium class (MED).

3.4. Fragility curves

For the investigated flow depths, the failure probability associated to a given pressure can be obtained by interpolating the obtained data. To get instead the failure probability for a given avalanche pressure for flow depths not herein considered, fragility curves were computed (Bachmann et al. 2013). To achieve such goal, the data herein obtained were fitted to a lognormal cumulative distribution function, as proposed by Shinozuka et al. (2000):

$$P_f(x, H) = \Phi\left(\frac{\ln x - \ln x_m(H)}{\beta(H)}\right), \tag{11}$$

where $P_f(x, H)$ is the probability that the element would fails if avalanche snow pressure is x and flow depth is H, Φ refers to the cumulative standard normal distribution. The terms x_m and β, which depend on the flow depth H, are the shape parameters of the distribution. In the lognormal distribution, x_m represents the median of the distribution, while β is the dispersion parameter, which represents the standard deviation (σ) in the logarithmic domain. The values of the parameters x_m and β for a given flow depth can be derived by linear interpolation of the corresponding x_m and β parameters obtained from the previous fittings. The parameters were computed for either dense-snow avalanches, or for saltation/powder avalanches against poles or towers. The validity of the extrapolation for dense snow avalanches is within the investigated flow-depths: [0.5, 5] m for wooden and steel poles, and [1.85, 4.7]m for towers.

4. Results

Snow avalanches are inherently variable phenomena. Multiple events may occur along the same path within a single season, each characterised by distinct release volumes, snow types (e.g. dry or wet), and flow regimes.

These initial conditions, combined with the spatial variability of snow cover along the track, lead to a wide range of flow velocities and bulk densities at the point of impact with the obstacle. Given this variability, flow velocity alone does not provide a sufficiently robust metric for characterising avalanche loading. In contrast, impact pressure, defined as a function of both velocity and density, offers a more comprehensive representation of the dynamic load exerted by the avalanche. For this reason, the curves presented in the following sections are plotted with respect to pressure rather than other flow variables. This approach is also consistent with established engineering and hazard assessment practices, where avalanche zoning and structural design criteria are typically based on expected impact pressures rather than flow velocities.

4.1. Poles

Figure 8 reports the graphs related to the failure probabilities for different impact pressures for steel and timber poles subjected to a dense-core avalanche having a flow depth of 1 m. The black dots refer to the value of the failure probability computed through Equation (9). Focussing on the steel poles, Figure 8(a), it is seen that for small impact pressures the failure probability is (almost) null. For impact pressures larger than 120kPa, the failure probability is one, meaning that all the analysed cases have shown forces that exceed the capacity of the system. The stacked coloured bars indicate the percentage of failures associated to each mode, pure bending or shear, or bending and shear. In steel poles and up 150 kPa, the cause of failure is associated to an acting bending moment that exceeds the bending capacity. For larger impact pressures, the shear failure also occurs. It is interesting to note that the latter failure only occurs in a limited fraction of the analysed cases. Timber poles experience a similar trend, as can be seen in Figure 8(b). The failure probability is non-null for pressures smaller if compared with the metallic cases. The bending failure is characteristic of impact pressures smaller than 80 kPa, while for larger figures bending and shear turn to be the predominant failure modes. In none of the cases the pure shear failure is observed.

The failure probabilities derived for steel and wooden poles subjected to dense snow avalanche loading are presented in Figure 9(a,b), respectively. The curves refer to the case $\lambda = 2.5$. These points have been obtained through analytical procedures and fitted using the lognormal distribution. The fitting allows for a continuous and smooth estimation of the failure probability as a function of avalanche pressure, overcoming the discontinuities observed in empirical data.

The two structural types exhibit different behaviours in terms of resistance. Steel poles demonstrate significantly higher performance, typically withstanding pressures ranging from 10 kPa up to 100 kPa. In contrast, wooden poles generally fail at lower pressures, rarely exceeding 80 kPa. The difference in performance

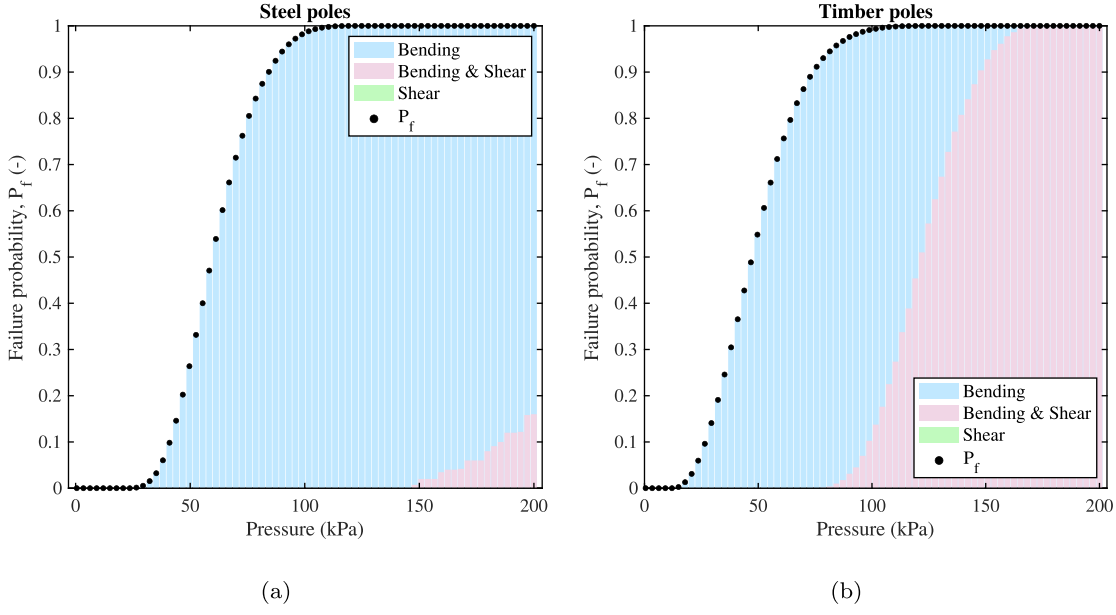

Figure 8. Modes associated to the failure. The total value fo the stacked bars correspond to the failure probability associated to each pressure. The height of the coloured bars is proportional to the percentage of cases associated to each failure mode. In the examined cases, shear failure does not occur. (a) Steel poles; (b) Timber poles.

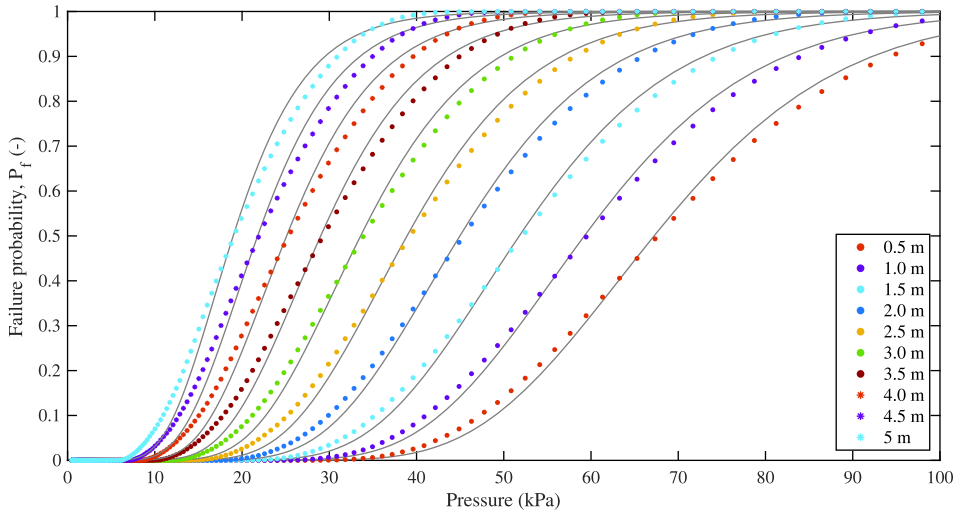

(a) Steel poles

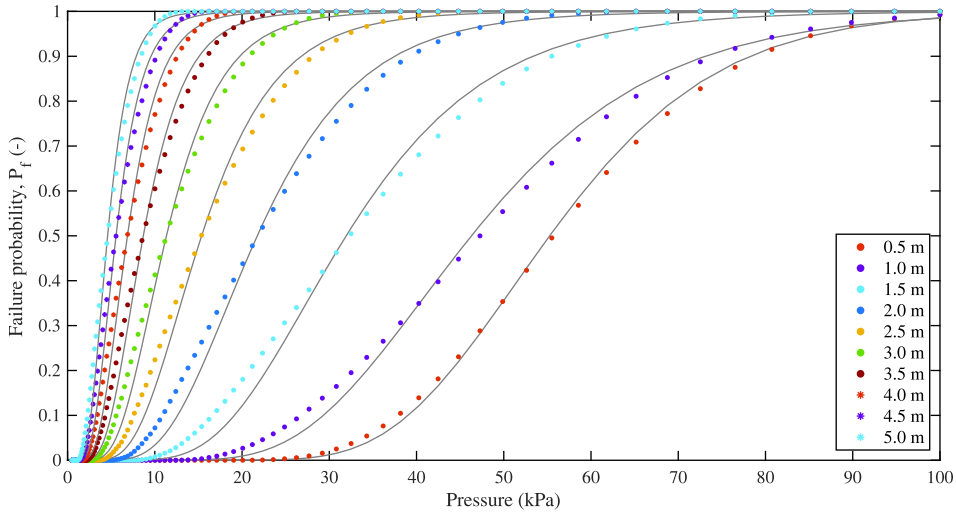

(b) Timber poles

Figure 9. Failure probabilities for steel and timber poles subjected to a dense snow avalanche ($\lambda = 2.50$). The scatter plots refer to specific flow depths (h_f), as detailed in the legend. The grey curves are the log-normal best fits. (a) Steel poles; (b) Timber poles.

becomes even more evident when analyzing the fragility curves at increasing avalanche flow depths. While both types of poles show a decrease in structural capacity with greater flow depth, the rate and extent of this degradation vary. Wooden poles are particularly sensitive to deep flows, showing a pronounced increase in failure probability at lower pressures. Steel poles, on the other hand, retain a more stable behaviour across the depth range, indicating greater strength. The steepness of the central portion of the fragility curves reveals an interesting trend: at high flow depths, timber poles exhibit a more rapid increase in failure probability compared to steel poles. This indicates a more abrupt transition from safe to failed conditions, highlighting their greater sensitivity to incremental increases in avalanche pressure.

The results of the analyses that include the saltation layer are reported in Figure 10. It clearly emerges that the saltation layer has a relevant effect in the failure probability. Taking the timber poles as examples, the failure is likely to occur more frequently even for low dense flow depths. This is due to the fact that the force due to saltation is applied at the top of the pole that is an unfavourable position. By examining the contour lines, it is worth noting that the effects of saltation and dense flow are contrasting. A contour line parallel to one axis denotes the low dependence of the failure probability on quantity plotted on the axis. Hence, it results that at low depths, the saltation plays the key role on P_f, while an opposite trend emerges for large flow depth, where the failure probability depends on the dense component impact pressure.

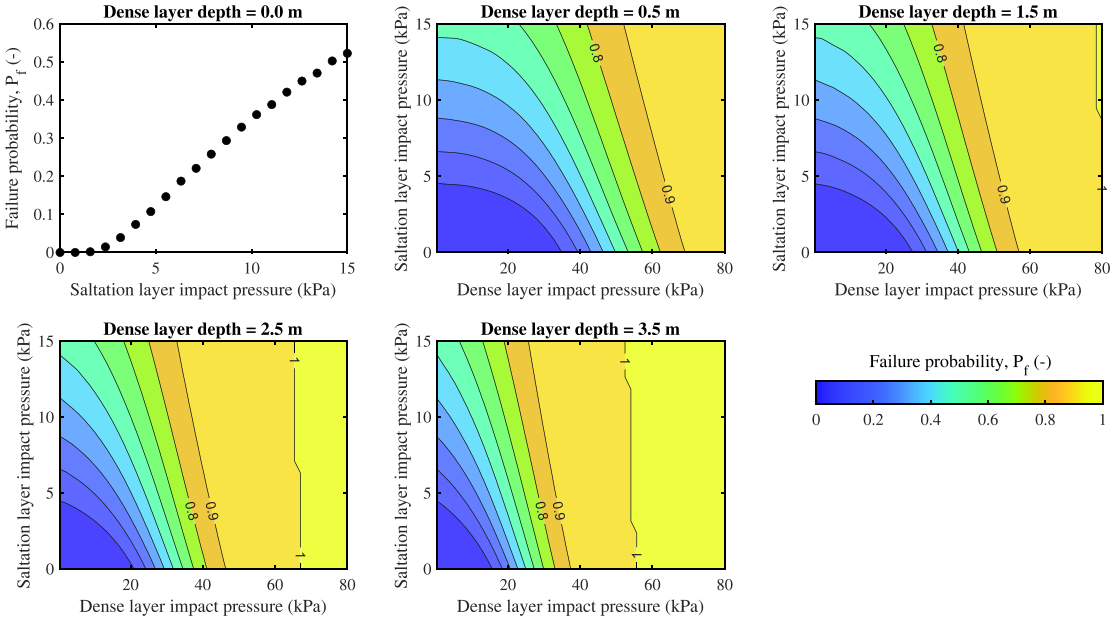

(a) Steel poles

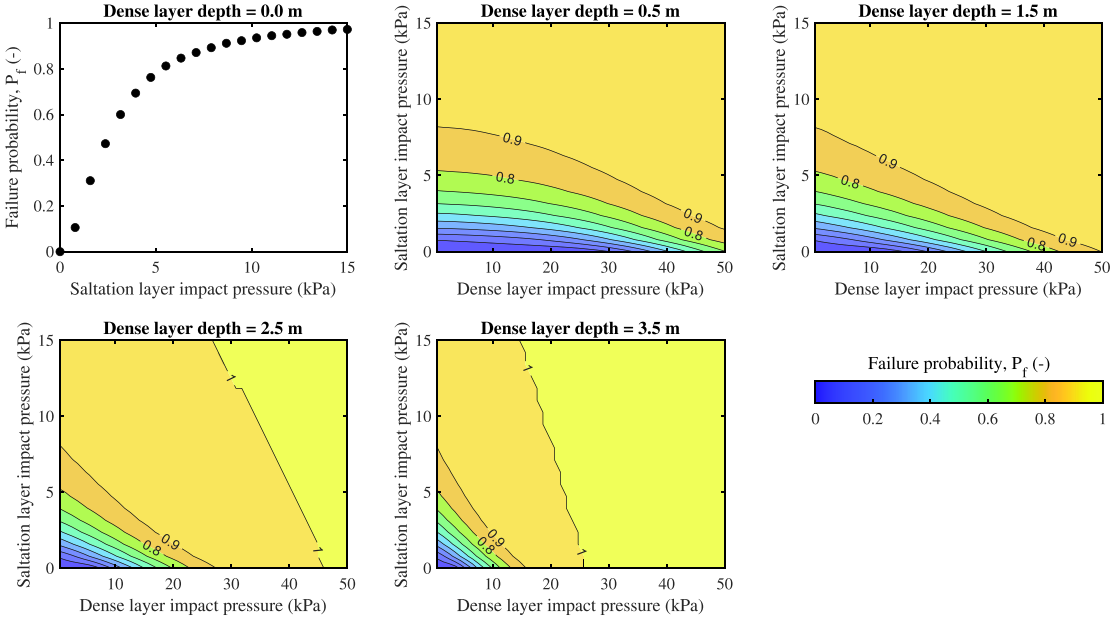

(b) Timber poles

Figure 10. Failure probabilities for steel and timber poles subjected to a dense dry-snow avalanche with a saltation layer. Top left plots refer to the case in which no dense component reaches the pole, the remaining contour plots relate to different dense component depths. For sake of clarity, the bounds for the dense layer impact pressure are set at 80 kPa and 50 kPa for (a) steel poles and (b) timber poles, respectively.

4.2. Towers

The results of the pushover analyses carried out on power transmission towers clearly highlight the progressive collapse mechanism typical of this type of structure. Among the simulations, the one identified by the name C-$h_{f,3}$ (see Table 9) with scaling factor SF = 1 was selected as the most representative and will be adopted as the reference model for interpreting the typical structural response of the towers. The outcomes of this analysis are discussed in detail in the following. In C-$h_{f,3}$ simulation, the avalanche flow is directed along the bisector of the x–y plane, corresponding to the AF-3 direction shown in Figure 6. Selected frames from this analysis are shown in Figure 11. The figure shows that as the flow pressure increases, following a linear trend with time, the tower begins to deform and gradually loses its initial configuration. Structural failure

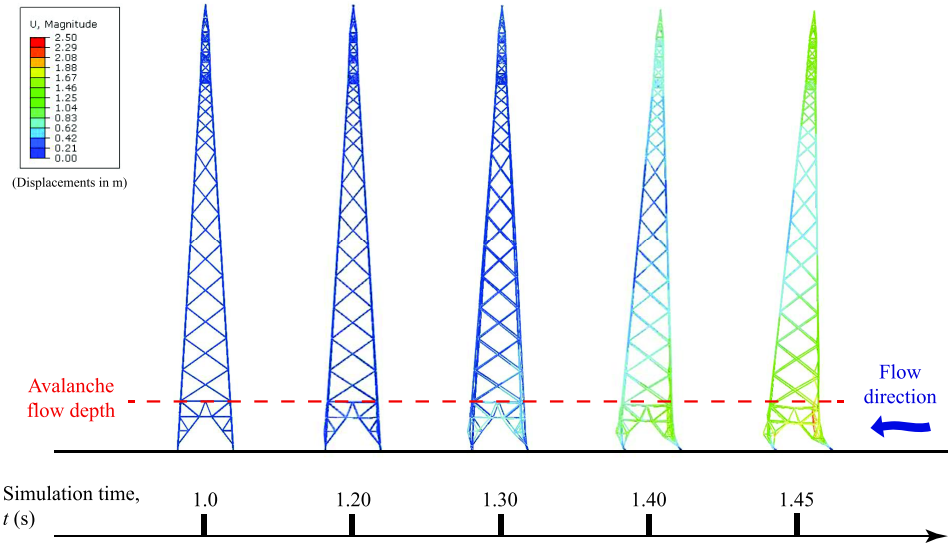

Figure 11. Selected frames from the C-$h_{f,3}$ simulation with SF = 1. The avalanche load, which increases linearly over time, is applied starting from $t = 1s$.

occurs at approximately 1.3 s (285 kN) of simulation time, when the structure starts to tilt and loses vertical alignment. From about 1.4 s (380 kN), a hinge-like behaviour develops at the base of the tower, indicating the onset of a global collapse mechanism.

Quantitative results from this simulation are presented in Figure 12. The displacement evolution of the tower top node is shown in Figure 12(a). Up to approximately 1.2 s (190 kN), the tower experiences minimal displacement. Beyond this point, a significant increase is observed in all the components of the displacement, ultimately leading to divergence of the numerical simulation near the end of the time history. This divergence is intentionally permitted in this type of analysis to capture the maximum load level the tower is capable of withstanding before collapse. In Figure 12(b) the sum of the reaction forces registered at the basis of the four legs of the tower is plotted against the displacement of the top node of the tower. It can be seen that, after an initial sharp increase of the force, starting from almost 0.2 m, large displacement occurs with reducing reaction force as a consequence of the loss of stability of the tower. In Figure 12(c), the total reaction force (defined as the sum of the x, y, and z components) is reported for the nodes located at the base of each of the four tower legs, as schematically shown in Figure 12(d). Among them, leg 3 (node 31), which is the most directly impacted by the avalanche, exhibits the highest reaction force, followed by leg 1 (node 22), located on the opposite side of the tower. Leg 3 reaches a peak force of approximately 750 kN at around 1.3 s, while leg 1 shows a slightly lower maximum of about 590 kN at approximately 1.2 s. The similar reaction-force evolution of these two legs reflects the symmetrical nature of the applied load. In contrast, legs 2 and 4 (nodes 11 and 30, respectively) experience significantly lower reaction forces, generally remaining below 200 kN. This suggests that the impact of the avalanche is not evenly distributed among the legs as the vertical forces resulting from bending dominate over the horizontal forces, with the structural demand being concentrated primarily on the frontally exposed ones. Interestingly, the drop in the reaction force on leg 1 after 1.25s is attributed to the onset of buckling on leg 1, which is compressed. The loading conditions and the slightly different arrangement of rods in the x and y directions, which result in different stiffnesses, induce minor torsional effects. These effects are visible in the gap between the curves of legs 2 and 4.

The mechanical behaviour of the tower legs is analysed in greater detail in Figure 13, which reports the axial forces acting on the elements of both the impacted and opposite legs with respect to the top displacement. To better assess the structural response, the axial forces are normalised by dividing them by the yield force of each element. The yield force is computed as the product of the steel yield stress and the element cross-sectional area. Positive values of the normalised axial force indicate elements under tension, while negative values correspond to those in compression. Elements 1 to 4 in the figure are positioned within the avalanche flow depth, while the remaining elements are located at higher levels. For the impacted leg, most elements remain in tension, except during the initial moments of the simulation when compression occurs due to the gravitational permanent loads acting on the tower. In

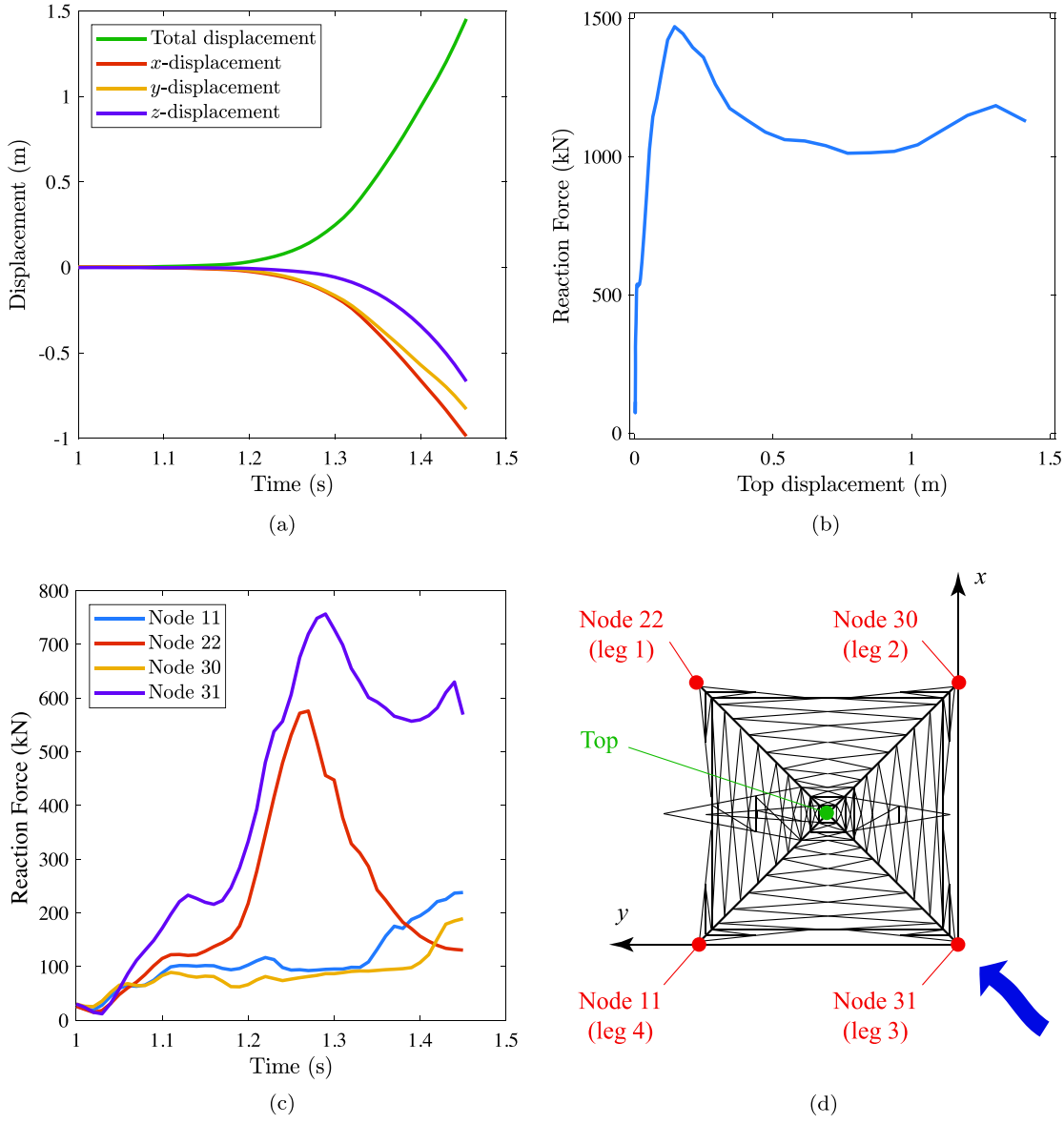

Figure 12. Results of the C-$h_{f,3}$ simulation, with SF = 1. (a) Displacement of the tower top vs. time; (b) Sum of the reaction force at the tower base vs. top displacement; (c) Reaction forces at the basis of the tower; (d) Scheme of the tower with names of the legs (the blue arrow shows the avalanche direction used in the considered simulation).

contrast, the opposite leg is primarily subjected to compression, with the exception of some elements near the top of the tower, which experience tension.

Figure 14 presents the fragility curves for the analysed set of power transmission towers. These curves represent the best-fit lognormal distributions derived from the numerical results, which are also displayed as scattered points for each corresponding flow depth and tower size. The results highlight a pronounced sensitivity of the towers to avalanche flow depth. When the flow depth reaches 4.70 m, nearly all towers collapse under pressures below 100 kPa, indicating a significant reduction in structural capacity under deep avalanche conditions. At an intermediate flow depth of 3.20 m, most towers fail under maximum pressures of approximately 160 kPa, confirming the inverse relationship between flow depth and resistance. Conversely, when the avalanche flow depth is below 1.85 m, the structural performance of the towers improves considerably. For instance, at a pressure level of around 200 kPa, only about 30% of the towers experience failure.

To conclude, the structural performance of the towers can be further assessed by referring to the different groups of load cases described in Table 9. In Figure 15(a), the avalanche-induced pressure is plotted against the corresponding top displacement. For clarity, only the case with the maximum flow depth (4.70 m) is shown. The results reveal that the most critical load cases are those

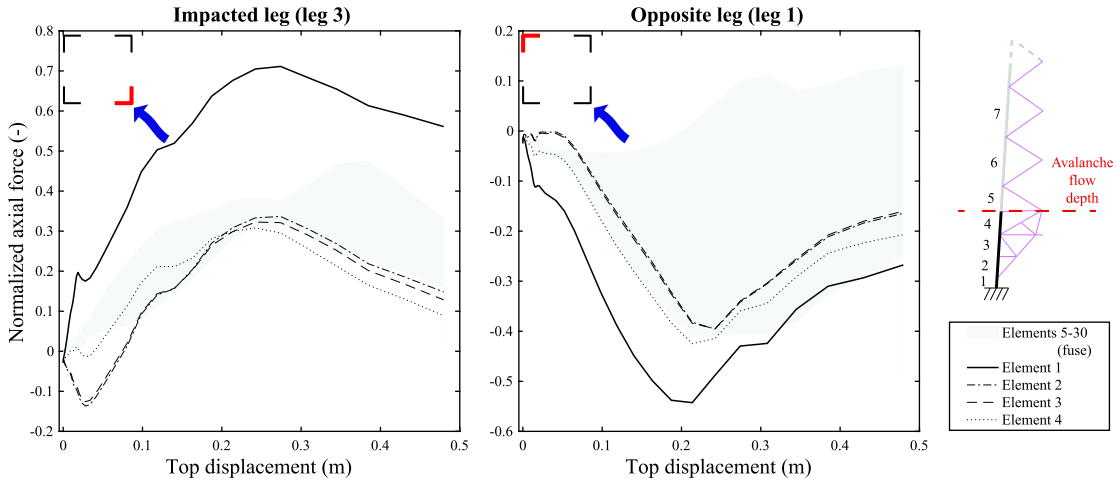

Figure 13. Normalised axial forces for the impacted leg of the tower (on the left) and the opposite leg (on the right). Different line styles refer to elements 1 to 4, which are the ones directly loaded by the avalanche. The grey area is a fuse of the curves related to elements from 5 to 30 that are the ones above the avalanche flow level.

in which the avalanche impacts the majority of the tower legs. This is evident in cases C4, C5, and especially in the generic case C, where three legs are simultaneously affected. In these scenarios, the maximum pressure sustainable by the structure drops significantly, reaching values as 30 kPa. Load cases A and B, where two legs are impacted, exhibit a similar response, withstanding pressures of approximately 50 kPa. Symmetric load configurations, such as A1 and A2 or B1 and B2, which share the same flow direction, demonstrate similar behaviour, withstanding pressures of up to 70 kPa.

In Figure 15(b), the pressure–top displacement curves are shown for different scaling factors (SF), all referring to the same load case, C-$h_{f,3}$. The results indicate that larger structures exhibit lower structural capacity compared to smaller ones. Notably, all curves share a similar initial behaviour, with differences becoming evident beyond a displacement of approximately 0.02 m. This trend reflects a common pattern also observed in the previous and following figure, where the initial portion of the curves overlaps across all cases, suggesting that the early structural response

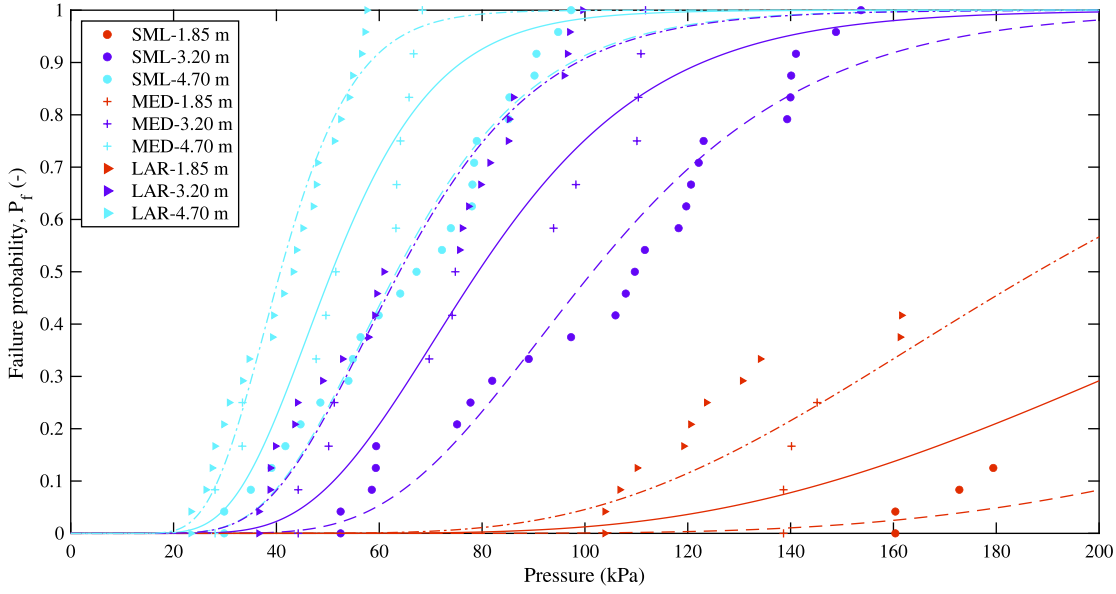

Figure 14. Failure probability for power transmission towers subjected to a dense snow avalanche. The scatter plots refer to specific flow depths (h_f) and tower size, as detailed in the legend. The coloured curves are the log-normal interpolations: the dashed line (- -) refer to the small (SML) tower, the continous line (–) to the medium (MED) tower, the dashed-dotted (-.) to the large (LAR) tower. For readability, the x-axis is bounded at 200 kPa.

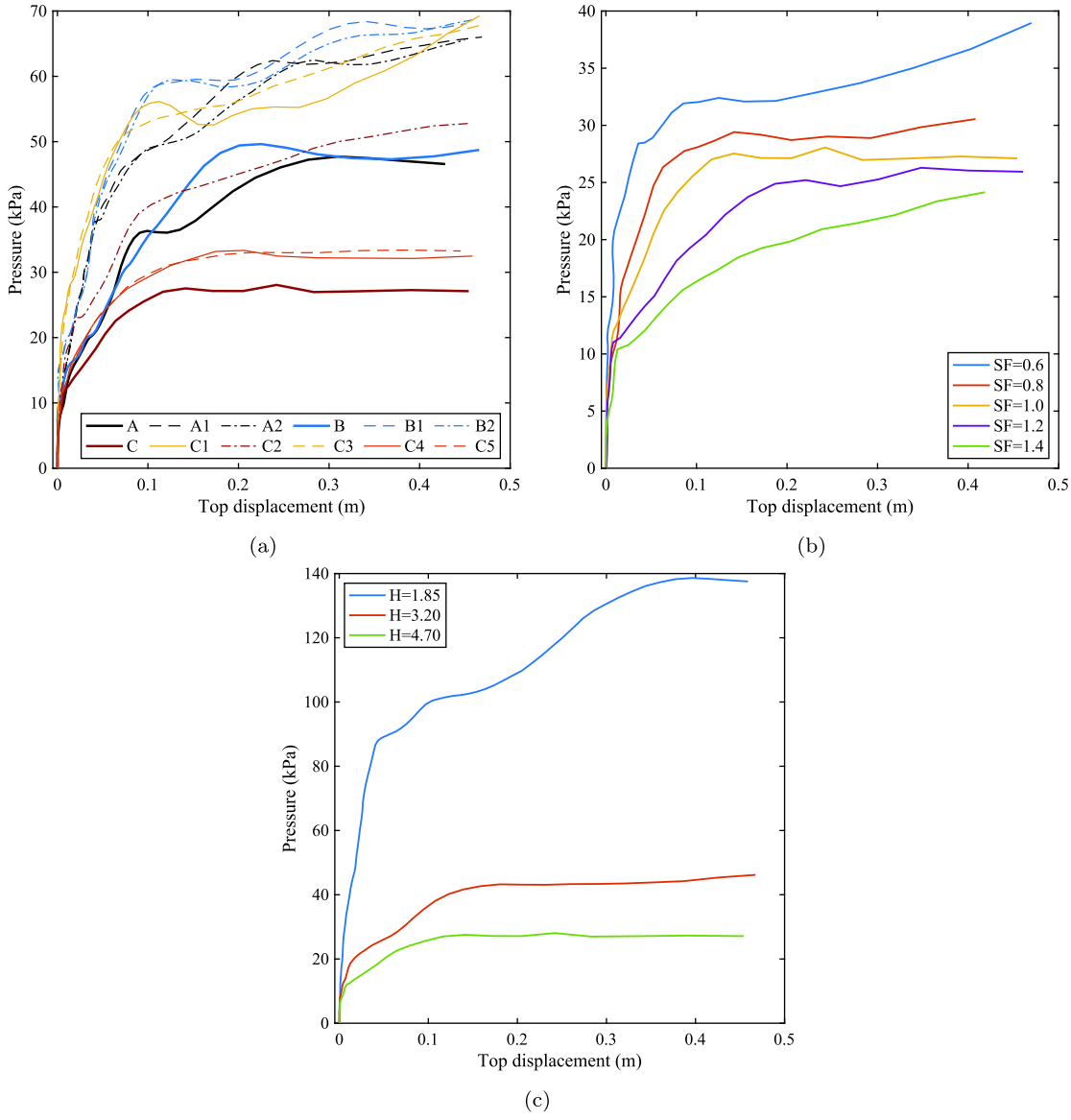

Figure 15. Strutural response of different groups of towers to avalanche load in terms of avalanche pressure vs. top displacement. (a) Differences among groups of load cases for the deepest flow (4.70 m); (b) Effect of the scaling factor for the case C-$h_{f,3}$; (c) Effect of the flow depth in case of load case C.

is not significantly influenced by the scale, while the nonlinear behaviour and failure onset are more sensitive to structural size.

The influence of flow depth is further illustrated in Figure 15(c), which clearly shows that higher avalanche flow depths are associated with a significant reduction in structural capacity. As in the previous analysis, the C load case is used as a reference. The figure highlights that, for a flow depth of 1.85 m, the structure is able to withstand pressures up to approximately 140 kPa. In contrast, this allowable pressure drops to about 50 kPa for a depth of 3.50 m, and further decreases to just 30 kPa when the flow depth reaches 4.70 m. These results highlight the strong inverse relationship between avalanche depth and the tower capacity, with the deepest flow causing a fivefold reduction in resistance compared to the shallowest case.

Table 10. Ultimate pressures for a medium size (MED) tower subjected to a powder snow avalanche.

Flow depth	AF-1	AF-2	AF-3
$1/3H_{tot}$	97.3 kPa	97.3 kPa	52.5 kPa
$2/3H_{tot}$	29.3 kPa	29.3 kPa	26.3 kPa
$3/3H_{tot}$	12.3 kPa	12.0 kPa	7.1 kPa

For powder avalanches, the ultimate pressures reported in Table 10 were obtained. It can be observed that cases AF-1 and AF-2 yield the same pressure, whereas the pressure for the AF-3 direction is lower.

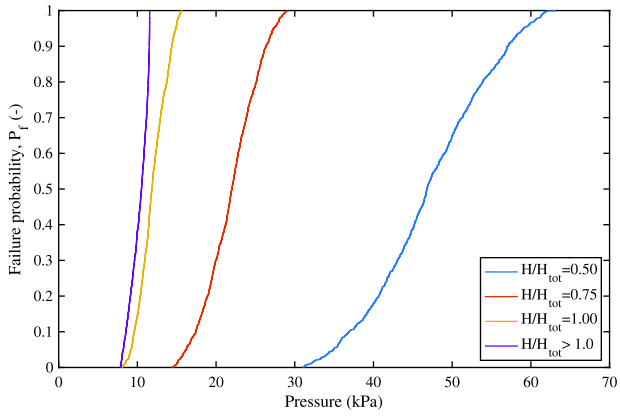

Figure 16. Failure probability for power transmission towers subjected to a powder snow avalanche. The curves refer to different flow depth, according to the normalised flow depth.

This reduction is due to the larger impacted surface, which increases the tower's vulnerability. For powder avalanches, the AF-1 and AF-2 loading directions can therefore be considered equivalent. The limit pressures, p_{lim}, obtained for the three depths were interpolated using a piecewise function in the form:

$$p_{lim}(H) = \begin{cases} A\, e^{-bH/H_{tot}}, & \text{if } H \le H_{tot} \\ C. & \text{if } H > H_{tot} \end{cases} \quad (12)$$

For AF-1 and AF-2 (impact angle equal to 0° or 90°) the following triad of parameters was obtained $(A, B, C) = (253864, 3.089, 11562)$, while for AF-3 it results $(A, B, C) = (155285, 2.986, 7840)$ (values in Pa). The interpolation with the impact angle was performed as:

$$p_{lim}(H, \alpha) = p_{lim}(H, AF1) - \left[p_{lim}(H, AF1) - p_{lim}(H, AF3)\right] \times \sin(2\alpha), \quad (13)$$

with $\alpha \in [0°, 90°]$.

The Monte Carlo sampling of flow depth and impact angle, as described in Section 3.3.2, produced the curves shown in Figure 16. The results indicate that the curve tends toward a vertical trend for flow depths exceeding the tower height.

Table 11. Parameters of the fragility curve for poles subjected to saltation, without dense component, and towers subjected to powder snow avalanches.

Type/flow depth	$\ln x_m$	β
		Poles
Steel	9.558	0.886
Timber	7.827	0.904
		Towers
0.50 H_{tot}	10.755	0.161
0.75 H_{tot}	9.993	0.149
1.00 H_{tot}	9.375	0.150
> 1.0 H_{tot}	9.219	0.114

Note: The tower cases refer to different cloud depth, from half tower height to a full interaction.

4.3. Parameters of the fragility curves

The comparison among different types of power transmission line supports subjected to dense snow avalanches is illustrated in Figure 17, where the shape parameters of the lognormal distribution ($\ln x_m$ and β) are plotted in a single graph against flow depth. These values correspond to the ones associated to the best-fitting lognormal distribution of the numerical data. Specifically, Figure 17(a) presents the graphs for $\ln x_m$.

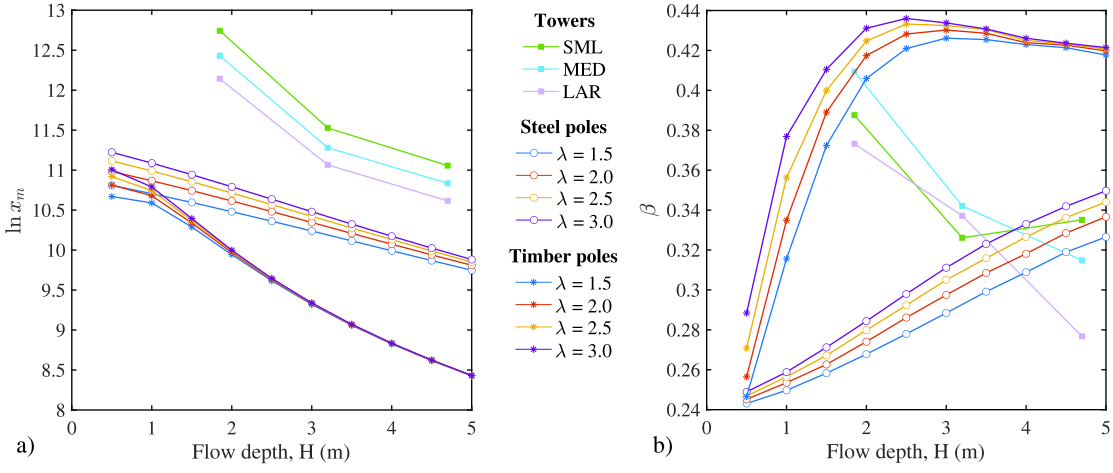

Figure 17. Graphs of the relationships between the shape parameters of the lognormal distribution and the flow depth for dense snow avalanches. (a) $\ln x_m$; (b) β.

For all types of supporting structures, the curves exhibit a strictly decreasing trend, indicating a higher structural capacity at lower flow depths. At shallow flow depths, steel and wooden poles exhibit comparable performance, with $\ln x_m \simeq 11$. However, as the avalanche flow depth increases, their responses begin to diverge markedly. Wooden poles show a pronounced increase in vulnerability, particularly beyond a depth of 1 m, where $\ln x_m$ drops sharply, indicating a significant reduction in structural capacity. The values for timber poles are almost irrespective of λ. In contrast, steel poles display a more stable and linear trend, maintaining higher values of $\ln x_m$ across the entire range of flow depths. In this case, the values depends on λ, with the dry-snow avalanches being the most severe, as the stagnation height is larger if compared with wet-snow avalanches. The data for towers exhibit the same decreasing trend but consistently maintain values above $\ln x_m \simeq 11$ across all flow depths for the three size classes, with larger towers exhibiting smaller $\ln x_m$.

The chart for β, see Figure 17(b), follows a distinct pattern, generally increasing with flow depth. However, steel poles display a linear trend and consistently lower values compared to other supporting systems. In contrast, the values for timber posts increase up to a flow depth of 2 m, after which they stabilise at approximately $\beta \simeq 0.45$). For steel poles, the dispersion of values due to the variability of λ remains almost constant across different flow depths, whereas for timber poles it progressively decreases. Towers exhibit a reduction in variability with increasing flow depth, which is nearly uniform across the three size classes.

The value of $\ln x_m$ and β for the saltation and powder effects on poles and towers, respectively, are reported in Table 11. Referring to poles, the values refer to the presence of the saltation layer, only. For the cases involving dense-core and saltation layer the failure probability must be obtained by the contour plots of Figure 10.

5. Conclusions

This study examines the structural vulnerability of power transmission line supports exposed to snow avalanche impacts, with a particular focus on developing fragility curves for commonly used support types, including wooden and steel poles as well as transmission towers.

The analyses focus on the impact of the dense core of snow avalanches and on the detrimental effect of saltation layers on lines and poles, and powder component on towers. To provide a quantitative assessment of their susceptibility to failure under varying avalanche conditions, analytical approaches are employed for poles, while a pushover FEM model is used for transmission towers. This assessment is based on different flow depths, allowing for a comprehensive evaluation of structural performance. Specifically, the study quantifies the probability of failure for a set of structures, considering variations in geometry and the dimensions of structural elements, and, in the tower transmission case, for different flow directions too.

The results highlight significant differences in the structural response of the analysed systems. Wooden poles exhibit the highest vulnerability, with failure occurring at relatively low avalanche pressures, while steel poles demonstrate greater capacity. Transmission towers, due to their more complex structural configuration and load redistribution mechanisms, display the highest capacity, withstanding significantly greater avalanche forces. However, their vulnerability remains non-negligible, particularly when subjected to powder snow avalanches.

The fragility curves developed in this study provide a valuable tool for assessing the probability of structural failure under different avalanche scenarios. These results have practical implications for risk assessment, structural design, and land-use planning in avalanche-prone areas. From a risk management perspective, this approach provides a rapid and reliable method to estimate the expected level of structural vulnerability in regions highly exposed to avalanche threats. This information is thus particularly valuable for policymakers, emergency planners, and infrastructure operators, enabling them to prioritise maintenance strategies, allocate resources effectively, and develop targeted mitigation measures to enhance the safety and reliability of power transmission networks.

Future research could further refine the accuracy of fragility curves by incorporating more detailed material models, accounting for snow-structure interaction effects, and considering alternative failure mechanisms such as progressive collapse. Experimental validation through field monitoring or controlled impact tests would further enhance the reliability of the proposed models.

Disclosure statement

No potential conflict of interest was reported by the author(s).

Funding

This publication is part of the project NODES which has received funding from the MUR– M4C2 1.5 of PNRR funded by the European Union – NextGenerationEU (Grant agreement no. ECS00000036). We acknowledge financial support under the National Recovery and Resilience Plan (NRRP), Mission 4, Component 2, Investment 1.1, Call for tender

No. 104 published on 2.2.2022 by the Italian Ministry of University and Research (MUR), funded by the European Union - NextGenerationEU- Project Title "A quantitative Framework for Structural Robustness Assessment" – CUP E53C24002780006 – Grant Assignment Decree No. 104 adopted on 02/02/2022 by the Italian Ministry of Ministry of University and Research (MUR).

ORCID

G. Vallero https://orcid.org/0000-0001-9731-8768
M. Marchelli http://orcid.org/0000-0002-9919-2916
V. De Biagi https://orcid.org/0000-0003-1866-9362

References

Albermani, F., S. Kitipornchai, and R. W. K. Chan. 2009. "Failure Analysis of Transmission Towers." *Engineering Failure Analysis* 16 (6): 1922–1928. https://doi.org/10.1016/j.engfailanal.2008.10.001.

Ancey, C. 2016. "Snow Avalanches." In *Oxford Research Encyclopedia of Natural Hazard Science*. Oxford, UK: Oxford University Press.

Anisha, A., A. Jacob, R. Davis, and S. Mangalathu. 2022. "Fragility Functions for Highway RC Bridge under Various Flood Scenarios." *Engineering Structures* 260:114244114244. https://doi.org/10.1016/j.engstruct.2022.114244.

Bachmann, D., N. Peter Huber, G. Johann, and H. Schüttrumpf. 2013. "Fragility Curves in Operational Dike Reliability Assessment." *Georisk: Assessment and Management of Risk for Engineered Systems and Geohazards* 7 (1): 49–60.

Barbero, M., F. Barpi, M. Borri-Brunetto, E. Bovet, B. Chiaia, V. De Biagi, B. Frigo. 2013. "A New Experimental Snow Avalanche Test Site at Seehore Peak in Aosta Valley (NW Italian Alps)–part II: Engineering Aspects." *Cold Regions Science and Technology* 86:14–21. https://doi.org/10.1016/j.coldregions.2012.10.014.

Bartelt, P., A. Caviezel, M. Christen, and O. Buser. 2020. "Impact of Hanging Cables and Power Transmission Lines by Mixed Flowing/powder Avalanches." In *25th International Conference on Theoretical and Applied Mechanics*, Milan, Italy.

Bertrand, D., M. Naaim, and M. Brun. 2010. "Physical Vulnerability of Reinforced Concrete Buildings Impacted by Snow Avalanches." *Natural Hazards and Earth System Sciences* 10 (7): 1531–1545. https://doi.org/10.5194/nhess-10-1531-2010.

Cai, Y., Q. Xie, S. Xue, L. Hu, and A. Kareem. 2019. "Fragility Modelling Framework for Transmission Line Towers under Winds." *Engineering Structures* 191:686–697. https://doi.org/10.1016/j.engstruct.2019.04.096.

Campbell, C., S. Conger, B. Gould, P. Haegeli, J. B. Jamieson, and G. Statham. 2016. "Technical Aspects of Snow Avalanche Risk Management–Resources and Guidelines for Avalanche Practitioners in Canada." *Revelstoke, BC, Canada* 15.

Caviezel, A., S. Margreth, K. Ivanova, B. Sovilla, and P. Bartelt. 2021. "Powder Snow Impact of Tall Vibrating Structures." In *8th ECCOMAS Thematic Conference on Computational Methods in Structural Dynamics and Earthquake Engineering, COMPDYN*, Athens, Greece, 5318–5330.

CEN. 2016. "EN 338:2016 Structural Timber – Strength Classes." European Committee for Standadization.

Christen, M., J. Kowalski, and P. Bartelt. 2010. "RAMMS: Numerical Simulation of Dense Snow Avalanches in Three-Dimensional Terrain." *Cold Regions Science and Technology* 63 (1-2): 1–14. https://doi.org/10.1016/j.coldregions.2010.04.005.

Dassault Systemes Simulia Corporation. 2011. *Abaqus 6.11*. Dassault Systemes Simulia Corporation.

De Biagi, V., B. Chiaia, and B. Frigo. 2015. "Impact of Snow Avalanche on Buildings: Forces Estimation from Structural Back-Analyses." *Engineering Structures* 92:15–28. https://doi.org/10.1016/j.engstruct.2015.03.004.

De Biagi, V., M. L. Napoli, and M. Barbero. 2017. "A Quantitative Approach for the Evaluation of Rockfall Risk on Buildings." *Natural Hazards* 88 (2): 1059–1086. https://doi.org/10.1007/s11069-017-2906-3.

Dunn, S., S. Wilkinson, D. Alderson, H. Fowler, and C. Galasso. 2018. "Fragility Curves for Assessing the Resilience of Electricity Networks Constructed from an Extensive Fault Database." *Natural Hazards Review* 19 (1):0401701904017019. https://doi.org/10.1061/(ASCE)NH.1527-6996.0000267.

Eckert, N., C. J. Keylock, D. Bertrand, E. Parent, T. Faug, P. Favier, and M. Naaim. 2012. "Quantitative Risk and Optimal Design Approaches in the Snow Avalanche Field: Review and Extensions." *Cold Regions Science and Technology* 79:1–19. https://doi.org/10.1016/j.coldregions.2012.03.003.

Eckert, Nicolas, M. Naaim, and E. Parent. 2010. "Long-Term Avalanche Hazard Assessment with a Bayesian Depth-Averaged Propagation Model." *Journal of Glaciology* 56 (198): 563–586. https://doi.org/10.3189/002214310793146331.

Favier, P., N. Eckert, T. Faug, D. Bertrand, I. Ousset, G. Candia, and J. Carlos de la Llera. 2022. "A Framework to Account for Structural Damage, Functional Efficiency and Reparation Costs within the Optimal Design of Countermeasures: Application to Snow Avalanche Risk Mitigation." *Cold Regions Science and Technology* 199:103559103559. https://doi.org/10.1016/j.coldregions.2022.103559.

Fu, X., H.-N. Li, L. Tian, J. Wang, and H. Cheng. 2019. "Fragility Analysis of Transmission Line Subjected to Wind Loading." *Journal of Performance of Constructed Facilities* 33 (4):0401904404019044. https://doi.org/10.1061/(ASCE)CF.1943-5509.0001311.

Gauer, P., D. Issler, K. Lied, K. Kristensen, and F. Sandersen. 2008. "On Snow Avalanche Flow Regimes: Inferences from Observations and Measurements." In *International Snow Science Workshop, Whistler, BC, Canada, 2008*.

Gaume, J., A. van Herwijnen, T. Gast, J. Teran, and C. Jiang. 2019. "Investigating the Release and Flow of Snow Avalanches at the Slope-Scale Using a Unified Model Based on the Material Point Method." *Cold Regions Science and Technology* 168:102847. https://doi.org/10.1016/j.coldregions.2019.102847.

Gazzetta Ufficiale della Repubblica Italiana. 2018. "Norme Tecniche per Le Costruzioni." *Decree of the Minister of the Infrastructures, D.M. 17/01/2018*.

Glade, T. 2003. "Vulnerability Assessment in Landslide Risk Analysis." *Die Erde; Zeitschrift der Gesellschaft für Erdkunde zu Berlin* 134 (2): 123–146.

Gorynina, O., and P. Bartelt. 2023. "Powder Snow Avalanche Impact on Hanging Cables." *International Journal of Impact Engineering* 173:104422104422. https://doi.org/10.1016/j.ijimpeng.2022.104422.

Gruber, U., and S. Margreth. 2001. "Winter 1999: a Valuable Test of the Avalanche-Hazard Mapping Procedure in Switzerland." *Annals of Glaciology* 32:328–332. https://doi.org/10.3189/172756401781819238.

Hofer, B., L. Schroll, and D. Illmer. 2019. "Everyday Work of an Avalanche Engineer–Calculation of Avalanche Loads and Protection of Small Objects in Avalanche Paths Like Ropeway Towers." In *Proceedings, International Snow Science Workshop*, Innsbruck, Austria, 2018.

Hopfinger, E. J. 1983. "Snow Avalanche Motion and Related Phenomena." *Annual Review of Fluid Mechanics* 15 (1): 47–76. https://doi.org/10.1146/fluid.1983.15.issue-1.

Jakob, M., D. Stein, and M. Ulmi. 2012. "Vulnerability of Buildings to Debris Flow Impact." *Natural Hazards* 60 (2): 241–261. https://doi.org/10.1007/s11069-011-0007-2.

Jóhannesson, T., P. Gauer, P. Issler, K. Lied, and K. M. Hákonardóttir. 2009. *The design of avalanche protection dams. Recent practical & theoretical developments*. Brussels: European Commission. ISBN: 978-92-79-08885-8.

Jones, K. W., G. J. Wolken, M. Janes, C. Wilbur, J. Glaus, P. Bartelt, and M. Christen. 2003. "Assessing Powder Cloud Impact on Electrical Transmission Lines at Snowslide Creek Avalanche Path in Southeast Alaska." In *Proceedings, International Snow Science Workshop*, Bend, Oregon, 2023.

Kiakojouri, F., V. De Biagi, Bernardino C., and Mohammad R. S.. 2020. "Progressive Collapse of Framed Building Structures: Current Knowledge and Future Prospects." *Engineering Structures* 206:110061110061. https://doi.org/10.1016/j.engstruct.2019.110061.

Kiakojouri, F., E. Zeinali, J. M. Adam, and V. De Biagi. 2023. "Experimental Studies on the Progressive Collapse of Building Structures: A Review and Discussion on Dynamic Column Removal Techniques." *Structures* 57:105059105059. https://doi.org/10.1016/j.istruc.2023.105059.

Kim, P., W. Seok Han, H. Kim, J. Hun Kim, and S. Kim. 2025. "Investigation of Load-Carrying Capacity and Failure Mechanisms in Full-Scale Testing of a re-fabricated Transmission Tower." *Engineering Failure Analysis* 171:109342109342. https://doi.org/10.1016/j.engfailanal.2025.109342.

Kyburz, M. L.. 2021. "Pressure on Obstacles Induced by Granular Snow Avalanches." PhD Diss., EPFL.

Li, X., B. Sovilla, C. Jiang, and J. Gaume. 2021. "Three-Dimensional and Real-Scale Modeling of Flow Regimes in Dense Snow Avalanches." *Landslides* 18 (10): 3393–3406. https://doi.org/10.1007/s10346-021-01692-8.

Lu, M. L., and D. Chakrabarti. 2022. "Designing Overhead Transmission Lines to Withstand Snow Avalanches." In *Electrical Transmission and Substation Structures 2022*, 223–234. Reston, VA: American Society of Civil Engineers.

Maggioni, M., M. Barbero, F. Barpi, M. Borri-Brunetto, V. De Biagi, M. Freppaz, B. Frigo, O. Pallara, and B. Chiaia. 2019. "Snow Avalanche Impact Measurements at the Seehore Test Site in Aosta Valley (NW Italian Alps)." *Geosciences* 9 (11): 471. https://doi.org/10.3390/geosciences9110471.

Margreth, S. 2007. *Defense Structures in Avalanche Starting Zones: Technical Guideline as an Aid to Enforcement*. Federal Office for the Environment FOEN.

Mayer, R., C. Plank, A. Bohner, S. Kollarits, A. Corsini, F. Ronchetti, H. Siegel. 2008. "Monitor: Hazard Monitoring for Risk Assessment and Risk Communication." *Georisk* 2 (4): 195–222.

McClung, D., and P. A. Schaerer. 1985. "Characteristics of Flowing Snow and Avalanche Impact Pressures." *Annals of Glaciology* 6:9–14. https://doi.org/10.3189/1985AoG6-1-9-14.

McClung, D., and P. A. Schaerer. 2006. *The Avalanche Handbook*. 3rd ed. Seattle: The Mountaineers Books. ISBN: 978-0898863642.

Mellor, M. 1978. "Dynamics of Snow Avalanches." *Developments in Geotechnical Engineering* 14:753–792. https://doi.org/10.1016/B978-0-444-41507-3.50031-3.

Naaim, M., T. Faug, and F. Naaim-Bouvet. 2003. "Dry Granular Flow Modelling including Erosion and Deposition." *Surveys in Geophysics* 24 (5-6): 569–585. https://doi.org/10.1023/B:GEOP.0000006083.47240.4c.

Naaim, M., F. Naaim-Bouvet, T. Faug, and A. Bouchet. 2004. "Dense Snow Avalanche Modeling: Flow, Erosion, Deposition and Obstacle Effects." *Cold Regions Science and Technology* 39 (2-3): 193–204. https://doi.org/10.1016/j.coldregions.2004.07.001.

Nishimura, K., H. Narita, N. Maeno, and K. Kawada. 1989. "The Internal Structure of Powder-Snow Avalanches." *Annals of Glaciology* 13:207–210. https://doi.org/10.3189/S0260305500007904.

Ousset, I., D. Bertrand, M. Brun, E. Thibert, A. Limam, and M. Naaim. 2015. "Static and Dynamic FE Analysis of an RC Protective Structure Dedicated to Snow Avalanche Mitigation." *Cold Regions Science and Technology* 112:95–111. https://doi.org/10.1016/j.coldregions.2014.12.013.

Pudasaini, S. P., and K. Hutter. 2007. *Avalanche Dynamics: Dynamics of Rapid Flows of Dense Granular Avalanches*. Berlin Heidelberg: Springer-Verlag. ISBN: 978-3-540-32686-1.

Rajkumari, S., K. Thakkar, and H. Goyal. 2022. "Fragility Analysis of Structures Subjected to Seismic Excitation: A State-of-the-art Review." *Structures* 40:303–316. https://doi.org/10.1016/j.istruc.2022.04.023.

Rao, N. Prasad, G. M. Samuel Knight, N. Lakshmanan, and Nagesh R. Iyer. 2010. "Investigation of Transmission Line Tower Failures." *Engineering Failure Analysis* 17 (5): 1127–1141. https://doi.org/10.1016/j.engfailanal.2010.01.008.

RAVA, Ufficio Neve e Valanghe. 2025. *Catasto Valanghe Regionale*. Technical Report. Regione Autonoma Valle d'Aosta. https://valangheweb.partout.it/.

Rudolf-Miklau, F., S. Sauermoser, and A. I. Mears. 2014. *The Technical Avalanche Protection Handbook*. Berlin: Wiley Online Library. ISBN: 978-3-433-03034-9.

Sampl, P., and M. Granig. 2009. "Avalanche Simulation with SAMOS-AT." In *Proceedings of the International Snow Science Workshop*, Davos, Vol. 27, 519–523.

Sampl, P., and T. Zwinger. 2004. "Avalanche Simulation with SAMOS." *Annals of Glaciology* 38:393–398. https://doi.org/10.3189/172756404781814780.

Schweizer, J., P. Bartelt, and A. van Herwijnen. 2021. "Snow Avalanches." In *Snow and Ice-Related Hazards, Risks, and Disasters*, 377–416. Amsterdam: Elsevier.

Shinozuka, M., M. Q. Feng, J. Lee, and T. Naganuma. 2000. "Statistical Analysis of Fragility Curves." *Journal of Engineering Mechanics* 126 (12): 1224–1231. https://doi.org/10.1061/(ASCE)0733-9399(2000)126:12(1224).

Sovilla, B., M. Schaer, and L. Rammer. 2008. "Measurements and Analysis of Full-Scale Avalanche Impact Pressure at the Vallée De La Sionne Test Site." *Cold Regions Science and Technology* 51 (2-3): 122–137. https://doi.org/10.1016/j.coldregions.2007.05.006.

Statham, G., P. Haegeli, E. Greene, K. Birkeland, C. Israelson, B. Tremper, C. Stethem, B. McMahon, B. White, and J. Kelly. 2018. "A Conceptual Model of Avalanche Hazard." *Natural Hazards* 90 (2): 663–691. https://doi.org/10.1007/s11069-017-3070-5.

Steer, P. J. 2001. "EN1995 Eurocode 5: Design of Timber Structures." In *Proceedings of the Institution of Civil Engineers-Civil Engineering*, Vol. 144, 39–43. London: Thomas Telford Ltd.

Tapia-Hernández, E., S. Ibarra-González, and D. De-León-Escobedo. 2017. "Collapse Mechanisms of Power Towers under Wind Loading." *Structure and Infrastructure Engineering* 13 (6): 766–782. https://doi.org/10.1080/15732479.2016.1190765.

Thibert, E., D. Baroudi, A. Limam, and P. Berthet-Rambaud. 2008. "Avalanche Impact Pressure on an Instrumented Structure." *Cold Regions Science and Technology* 54 (3): 206–215. https://doi.org/10.1016/j.coldregions.2008.01.005.

Vallero, G., V. De Biagi, M. Barbero, M. Castelli, and M. L. Napoli. 2020. "A Method to Quantitatively Assess the Vulnerability of Masonry Structures Subjected to Rockfalls." *Natural Hazards* 103 (1): 1307–1325. https://doi.org/10.1007/s11069-020-04036-2.

Van Westen, C. J., E. Castellanos, and S. L. Kuriakose. 2008. "Spatial Data for Landslide Susceptibility, Hazard, and Vulnerability Assessment: An Overview." *Engineering Geology* 102 (3-4): 112–131. https://doi.org/10.1016/j.enggeo.2008.03.010.

Wojciechowska, K., G. Pleijter, M. Zethof, F. J. Havinga, D. H. Van Haaren, and W. L. A. Ter Horst. 2015. "Application of Fragility Curves in Operational Flood Risk Assessment." In *Geotechnical Safety and Risk V*, 528–534. Amsterdam: IOS Press.

Yu, H., H. Li, Z.-Q. Zhang, G.-F. Zhang, D.-H. Wang, and H.-D. Zheng. 2022. "Failure Patterns of Transmission Tower-Line System Caused by Landslide Events." *Energies* 15 (19): 7155. https://doi.org/10.3390/en15197155.

Zhang, L., B. Xu, and D. Wang. 2024. "Coupled SPH-FEM Analysis of Piled Power Transmission Tower System Subjected to Debris Flow." *Computers and Geotechnics* 168:106176. https://doi.org/10.1016/j.compgeo.2024.106176.

Zhang, W., J. Zhu, H. Liu, and H. Niu. 2015. "Probabilistic Capacity Assessment of Lattice Transmission Towers under Strong Wind." *Frontiers in Built Environment* 1: 20. https://doi.org/10.3389/fbuil.2015.00020.